

1 **Production of protons, deuterons and tritons in**
2 **argon-nucleus interactions at 3.2A GeV**

3 BM@N Collaboration

4 **Abstract**

5 Results of the BM@N experiment at the Nuclotron/NICA complex are pre-
6 sented on proton , deuteron and triton production in interactions of an argon
7 beam of 3.2A GeV with fixed targets of C, Al, Cu, Sn and Pb. Transverse
8 mass spectra, rapidity distributions and multiplicities of protons, deuterons
9 and tritons are measured. The results are treated within a coalescence ap-
10 proach and compared with predictions of theoretical models and with other
11 measurements.

1 Introduction

BM@N (Baryonic Matter at Nuclotron) is the first operational experiment at the Nuclotron/NICA accelerator complex. The Nuclotron provides beams of a variety of particles, from proton up to gold ions, with kinetic energy in the range from 1 to 6 GeV/nucleon for light ions with Z/A ratio of ~ 0.5 and up to 4.5 GeV/nucleon for heavy ions with Z/A ratio of ~ 0.4 . At these energies, the nucleon density in the fireball created in the collisions of a heavy-ion beam with fixed targets is 3-4 times higher than the nuclear saturation density [1], thus allowing studying heavy-ion interactions in the regime of high-density baryonic matter [2–5].

In the commissioning phase, in a configuration with limited phase-space coverage, BM@N collected first data with beams of carbon, argon, and krypton ions [6, 7]. In the first physics paper BM@N reported on studies of π^+ and K^+ production in argon-nucleus interactions [8]. This paper presents results on proton, deuteron and triton production in 3.2A GeV argon-nucleus interactions.

At the Nuclotron energies, baryon transfer over finite rapidity distances (baryon stopping [9]) plays an important role [10]– [12]. The baryon density, attained in high energy nuclear collisions, is a crucial quantity governing the reaction dynamics and the overall system evolution, including eventual phase transitions. The baryon rapidity distributions in heavy ion collisions for different combinations of projectile and target as well as at different impact parameters provide essential constraints on the dynamical scenarios of baryon stopping. The BM@N experimental arrangement makes it possible to measure the distribution of protons and light nuclei (d, t) over the rapidity interval [1.0 - 2.2]. This rapidity range is wide enough to include not only the midrapidity ($y_{CM} = 1.08$), but also the beam rapidity region ($y_{beam} = 2.16$), in contrast to the collider experiments, where the acceptance is usually focused only in the mid-rapidity region. Together with a sufficient p_T -coverage for nuclear clusters, it is possible at BM@N to better determine the shape of the rapidity density distribution and derive information about rapidity and energy loss in the reaction.

Nuclear cluster production allows one to estimate the nucleon phase-space density attained in the reaction [13]. It governs the overall evolution of the reaction process and may provide information about freeze-out conditions and entropy production in relativistic nucleus-nucleus interactions. A way to measure the nucleon phase-space density is a study of the ratio of deuteron and proton abundances. One of the goals of this work is a study of particle phase-space density evolution in Ar+A collisions for different projectile-target combinations and as a function of collision centrality.

49 In the framework of statistical thermal models, hadron and light nuclei abun-
50 dances are predicted to be dependent on the bulk parameters of the fireball: the
51 freeze-out temperature T and baryochemical potential μ [14]. The ratio μ/T can
52 be extracted from the characteristic parameter (penalty factor) describing the mass
53 dependence of the cluster yield [15]. In this paper, we study the system size and
54 mass dependence of cluster production to get insight into the thermal parameters
55 of the particle source.

56 In collisions of heavy nuclei at relativistic energies, a significant fraction of the
57 initial kinetic energy transforms into particle production and thermal excitation of
58 matter. Various dynamical models, including those based on hydrodynamics, have
59 demonstrated that the entropy per baryon, S/A , created during the initial interac-
60 tion stage remains constant during the subsequent evolution of the system [16, 17].
61 Thus, data about entropy production can provide information not only about the
62 nucleon phase-space density at the final moments of the reaction (freezeout), but
63 also about the medium properties during the hot and compressed stage. It is also
64 the aim of this work to study the evolution of the entropy in the reaction zone with
65 system size in argon-nucleus collisions and compare BM@N results with other
66 existing experimental data.

67 The binding energies of deuterons and tritons are small compared to freeze-
68 out temperatures, which are on the order of 100 MeV. These light clusters are
69 therefore not expected to survive through the high density stages of the collision.
70 The deuterons and tritons observed in the experiment are formed and emitted at
71 the end of freeze-out process, and they mainly carry information about this late
72 stage of the collision.

73 Light cluster production at low energy heavy ion collisions is well described in
74 a simple coalescence model [18–21] through the distributions of their constituents
75 (protons and neutrons) and a coalescence parameter B_A related to the size A of the
76 cluster. To describe heavy-ion collisions at high energies the simple coalescence
77 model is modified taking into account the nucleon phase space distributions at
78 freeze-out as well as the strength of momentum-space correlations induced by
79 collective flow [22]. In central heavy-ion collisions the pressure gradient in the
80 system generates strong transverse radial flow. Therefore nucleon clusters inside a
81 collective velocity field acquire additional momentum proportional to the cluster's
82 mass.

83 The paper is organized as follows. Section 2 describes the experimental set-up
84 and Section 3 is devoted to details of the event reconstruction. Section 4 describes
85 the evaluation of the proton, deuteron and triton reconstruction efficiency. Sec-
86 tion 5 explains the methodology for the definition of centrality classes. Section 6

87 addresses the evaluation of the cross sections, multiplicities and systematic uncer-
 88 tainties. Transverse mass distributions and rapidity spectra of protons, deuterons
 89 and tritons are given in Section 7. The BM@N results are compared with pre-
 90 dictions of the DCM-SMM [23, 24] and PHQMD [25] models. Ratios of the
 91 transverse momentum distributions of deuterons and tritons to protons are treated
 92 within a coalescence approach in Section 8. The results are compared with other
 93 experimental data on nucleus-nucleus interactions. Results on baryon rapidity loss
 94 in argon-nucleus interactions are presented in Section 9. The compound ratios of
 95 yields of protons and tritons to deuterons are presented in section 10. Finally, a
 96 summary is given in Section 11.

97 2 Experimental set-up

98 The BM@N detector is a forward spectrometer covering the pseudorapidity range
 99 $1.6 \leq \eta \leq 4.4$. A schematic view of the BM@N setup in the argon-beam run is
 100 shown in Fig. 1. More details of all components of the set-up can be found in [26,
 101 27]. The spectrometer includes a central tracking system consisting of 3 planes of
 102 forward silicon-strip detectors (ST) and 6 planes of detectors based on gas electron
 103 multipliers (GEM) [28]. The central tracking system is located downstream of the
 104 target region inside of a dipole magnet with a bending power of about 2.1Tm and
 105 with a gap of 1.05 m between the poles. In the measurements reported here, the
 106 central tracker covered only the upper half of the magnet acceptance.

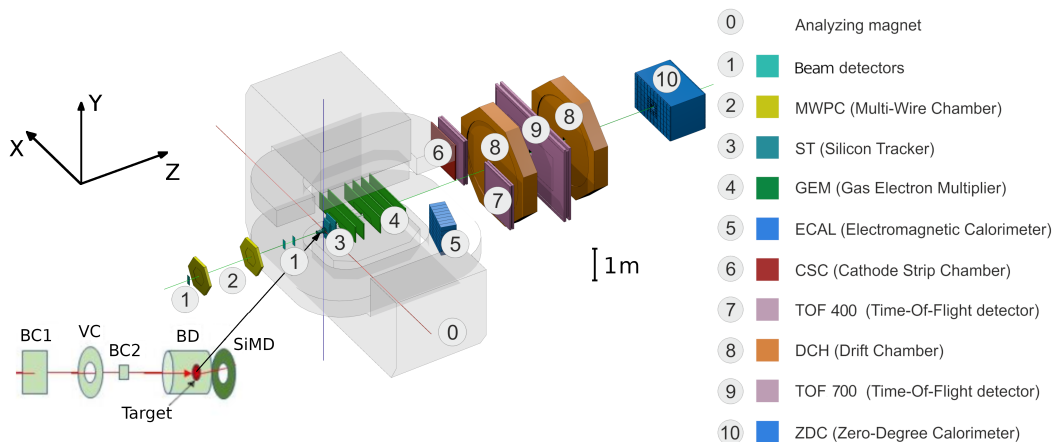


Figure 1: Schematic view of the BM@N setup in the argon beam run.

107 Two sets of drift chambers (DCH), a cathode strip chamber (CSC), two sets
108 of time-of-flight detectors (ToF), and a zero-degree calorimeter (ZDC) are located
109 downstream of the dipole magnet. The tracking system measures the momentum
110 of charged particles with a relative uncertainty that varies from 2.5% at a momen-
111 tum of 0.5 GeV/c to 2% from 1 to 2 GeV/c and rises linearly to 6.5% at 5 GeV/c.
112 The time resolutions of the ToF-400 [29] and ToF-700 [30] systems are 84 ps and
113 115 ps, respectively [31].

114 Two beam counters (BC1, BC2), a veto counter (VC), a barrel detector (BD),
115 and a silicon multiplicity detector (SiMD) are used for event triggering and for
116 measurement of the incoming beam ions. The BC2 counter provides also the
117 start time T0 for the time-of-flight measurement. The BD detector consists of 40
118 azimuthal scintillating strips arranged around the target, and the SiMD detector
119 consists of 60 azimuthal silicon segments situated behind the target.

120 Data were collected with an argon beam intensity of a few 10^5 ions per spill
121 and a spill duration of 2–2.5 sec. The kinetic energy of the beam was 3.2A GeV
122 with a spread of about 1%. A set of solid targets of various materials (C, Al,
123 Cu, Sn, Pb) with an interaction length of 3% was used. The experimental data
124 correspond to a total integrated luminosity of $7.8 \mu\text{b}^{-1}$ collected with the different
125 targets: $2.1 \mu\text{b}^{-1}$ (C), $2.3 \mu\text{b}^{-1}$ (Al), $1.8 \mu\text{b}^{-1}$ (Cu), $1.1 \mu\text{b}^{-1}$ (Sn), $0.5 \mu\text{b}^{-1}$ (Pb).
126 A total of 16.3M argon-nucleus collisions at 3.2A GeV were reconstructed.

127 To count the number of beam ions that passed through the target, a logical
128 beam trigger $\text{BT} = \text{BC1} \wedge \overline{\text{VC}} \wedge \text{BC2}$ was used. The following logic conditions were
129 applied to generate the trigger signal: 1) $\text{BT} \wedge (\text{BD} \geq 3, 4)$; 2) $\text{BT} \wedge (\text{SiMD} \geq 3, 4)$;
130 3) $\text{BT} \wedge (\text{BD} \geq 2) \wedge (\text{SiMD} \geq 3)$. The trigger conditions were varied to find the
131 optimal ratio between the event rate and the trigger efficiency for each target.
132 Trigger condition 1 was applied for 60% of the data collected with the carbon
133 target. This trigger fraction was continuously reduced with the atomic weight
134 of the target down to 26% for the Pb target. The fraction of data collected with
135 trigger condition 2 was increased from 6% for the carbon target up to 34% for the
136 Pb target. The rest of the data were collected with trigger condition 3.

137 **3 Event reconstruction**

138 Track reconstruction in the central tracker is based on a “cellular automaton” ap-
139 proach [32] implementing a constrained combinatorial search of track candidates
140 with their subsequent fitting by a Kalman filter to determine the track parameters.
141 These tracks are used to reconstruct primary and secondary vertices as well as

142 global tracks by extrapolation and matching to hits in the downstream detectors
143 (CSC, DCH and ToF).

144 The primary collision vertex position (PV) is measured with a resolution of
145 2.4 mm in the X-Y plane perpendicular to the beam direction and 3 mm in the
146 beam direction.

147 Charged particles (protons, deuterons, tritons) are identified using the time of
148 flight Δt measured between T0 and the ToF detectors, the length of the trajectory
149 Δl and the momentum p reconstructed in the central tracker. Then the squared
150 mass M^2 of the particle is calculated by the formula: $M^2 = p^2((\Delta t c / \Delta l)^2 - 1)$,
151 where c is the speed of light.

152 The following criteria are required for selecting proton, deuteron and triton
153 candidates:

- 154 • Each track has at least 4 hits in the GEM detectors (6 detectors in total) [28].
155 Hits in the forward silicon detectors are used to reconstruct the track, but no
156 requirements are applied to the number of hits.
- 157 • Tracks originate from the primary vertex. The deviation of the reconstructed
158 vertex from the nominal target position Z_{ver} along the beam direction is
159 limited to $-3.4 \text{ cm} < Z_{\text{ver}} - Z_0 < 1.7 \text{ cm}$. The upper limit corresponds to
160 $\sim 5.7\sigma$ of the Z_{ver} spread and cuts off interactions with the trigger detector
161 located 3 cm behind the target. The beam interaction rate with the trigger
162 detector is well below 1% and was not simulated since it does not affect the
163 precision in Monte Carlo simulation.
- 164 • Distance from the track to the primary vertex in the X-Y plane at Z_{ver} (DCA)
165 is required to be less than 1 cm, which corresponds to 4σ of the vertex
166 residual distribution in the X-Y plane.
- 167 • Momentum range of positively charged particles is limited by the accep-
168 tance of the ToF-400 and ToF-700 detectors to $p > 0.5 \text{ GeV}/c$ and $p > 0.7$
169 GeV/c , respectively.
- 170 • Distance of extrapolated tracks to the CSC (DCH) hits as well as to the ToF-
171 400 (ToF-700) hits should be within $\pm 2.5\sigma$ of the momentum dependent
172 hit-track residual distributions.

173 The mass squared (M^2) spectra of positively charged particles produced in in-
174 teractions of the 3.2A GeV argon beam with various targets are shown in Figs. 2a
175 and 2b for ToF-400 and ToF-700 data, respectively. Particles that satisfy the

176 above selection criteria contribute to the M^2 spectra. The proton, deuteron and
 177 triton signals are extracted in the M^2 windows which depend on rapidity and at
 178 the maximal rapidity extend from 0.4-1.7 $(\text{GeV}/c^2)^2$, 2.3-5.0 $(\text{GeV}/c^2)^2$ and 6.6-
 179 10.0 $(\text{GeV}/c^2)^2$, respectively. The signals of protons, deuterons and tritons and
 180 their statistical errors are calculated according to the formulae: $sig = hist - bg$,
 181 $err_{stat} = \sqrt{hist + \delta bg}$, where $hist$ denotes the histogram integral yield within the
 182 selected M^2 -window and δbg is the background normalization uncertainty.

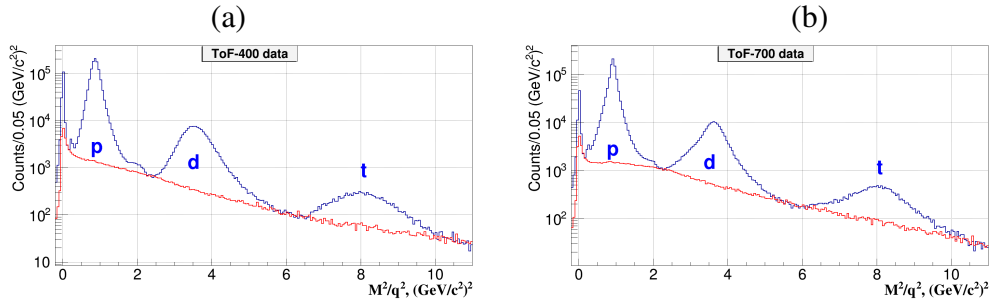


Figure 2: M^2/q^2 spectra of positively charged particles produced in argon-nucleus interactions and measured in the ToF-400 (a) and ToF-700 (b) detectors. Peaks of protons, deuterons, and tritons with the charge $q = 1$ are indicated; the small peaks of He fragments with $q = 2$ either overlap with the deuteron one (He^4) or show up at $M^2/q^2 \sim 2 (\text{GeV}/c^2)^2$ (He^3). The red histograms show the background estimated from “mixed events”.

183 The shape of the background under the proton, deuteron and triton signals in
 184 the M^2 spectra is estimated using the “mixed event” method. For that, tracks re-
 185 constructed in the central tracker are matched to hits in the ToF detectors taken
 186 from different events containing a similar number of tracks. The “mixed event”
 187 background is normalized to the integral of the signal histogram outside the M^2
 188 windows of protons, deuterons and tritons. It is found that the background level
 189 differs for light and heavy targets and for different intervals of rapidity and trans-
 190 verse momentum.

191 The ToF-400 and ToF-700 detectors cover different ranges of rapidity and
 192 transverse momentum of detected particles. Fig. 3 shows the deuteron signals
 193 measured in ToF-400 and ToF-700 in the rapidity vs transverse momentum plane
 194 in Ar+Sn interactions before making efficiency corrections.

195 The dE/dx information from the GEM detectors is used to separate the deuteron
 196 signals from the overlapping TOF He^4 signals. The fraction of He^4 in the total
 197 $He^4 + d$ sample is determined in rapidity and transverse momentum bins and sub-

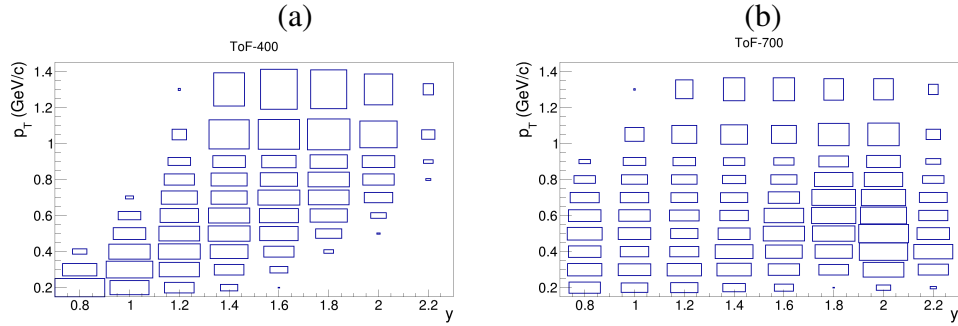


Figure 3: Distribution of the deuteron signals measured in ToF-400 (a) and ToF-700 (b) in the rapidity vs transverse momentum plane in Ar+Sn interactions.

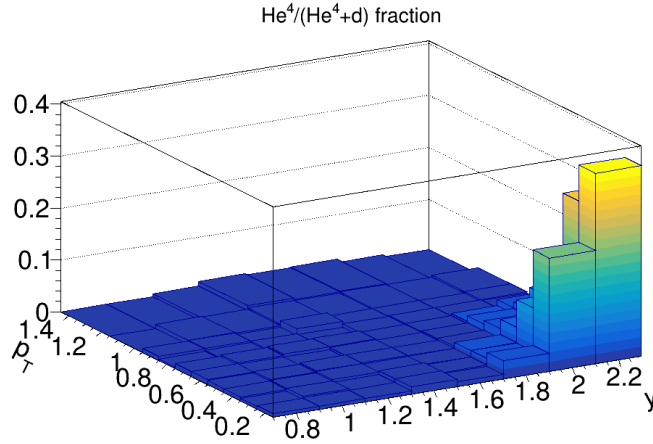


Figure 4: Fraction of He^4 in the $He^4 + d$ sample measured in the rapidity vs transverse momentum plane in Ar+A interactions.

198 tracted from the deuteron TOF signals. The He^4 fraction combined for all the
 199 targets is presented in Fig. 4. In most of the $y - p_T$ bins the He^4 fraction does not
 200 exceed 3%, only in a few bins at large y and low p_T it reaches 20-35%.

201 4 Reconstruction efficiency and trigger performance

202 To evaluate the proton, deuteron and triton reconstruction efficiency, Monte Carlo
 203 data samples of argon-nucleus collisions were produced with the DCM-SMM
 204 event generator. Propagation of particles through the entire detector volume and
 205 responses of the detectors were simulated using the GEANT3 program [33] inte-
 206 grated into the BmnRoot software framework [34].

207 The Monte Carlo events passed through the same chain of reconstruction and
 208 identification as the experimental ones. The efficiencies of the silicon, GEM,
 209 CSC, DCH and ToF detectors were adjusted in the simulation in accordance with
 210 the measured detector efficiencies [35]. More details of the simulation are given
 211 in ref. [8].

212 The proton, deuteron and triton reconstruction efficiencies are calculated in
 213 intervals of rapidity y and transverse momentum p_T . The reconstruction efficiency
 214 includes geometrical acceptance, detector efficiency, kinematic and spatial cuts,
 215 and the loss of protons, deuterons and tritons due to in-flight interactions. Figure 5
 216 shows the reconstruction efficiencies of protons (left panels) and deuterons (right
 217 panels) in ToF-400 and ToF-700 as functions of y (upper panels) and p_T (lower
 218 panels) for Ar+Sn interactions.

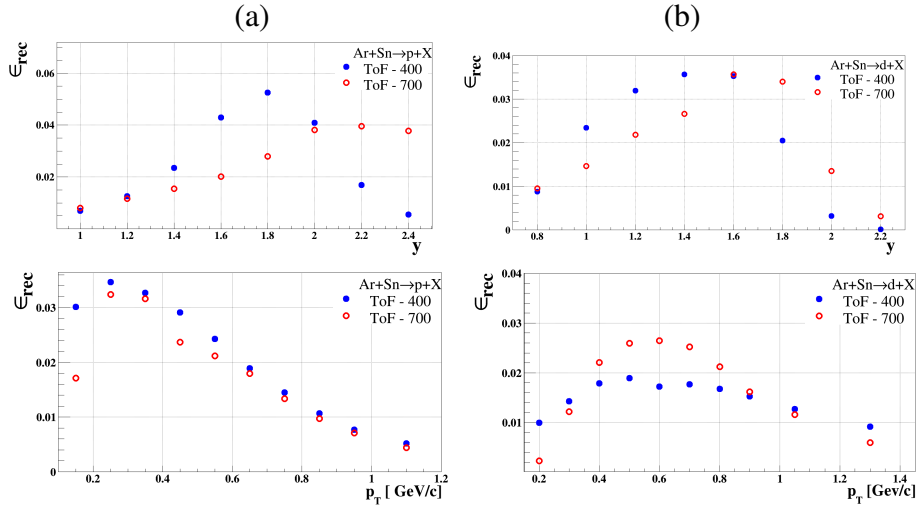


Figure 5: Reconstruction efficiency of protons (a) and deuterons (b) produced in Ar+Sn collisions, detected in ToF-400 (full blue circles) and ToF-700 (open red circles) as functions of rapidity y and p_T . The efficiency includes both acceptance and reconstruction.

219 The trigger efficiency ϵ_{trig} depends on the number of fired channels in the BD
 220 (SiMD) detectors. It was calculated for events with reconstructed protons, deuterons
 221 and tritons using event samples recorded with an independent trigger based on
 222 the SiMD (BD) detectors. The BD and SiMD detectors cover different and non-
 223 overlapping regions of the BM@N acceptance, that is, they detect different colli-
 224 sion products.

225 The efficiency of the combined BD and SiMD triggers was calculated as the

226 product of the efficiencies of the BD and SiMD triggers. The trigger efficiency
 227 decreases with a decrease in the mass of the target and an increase in the centrality
 228 of the collision. More details of the trigger efficiencies evaluation are given in
 229 ref. [8]. In particular, the trigger system accepts events in the whole centrality
 230 range, as it is illustrated in Fig. 10 of [8].

231 5 Centrality classes

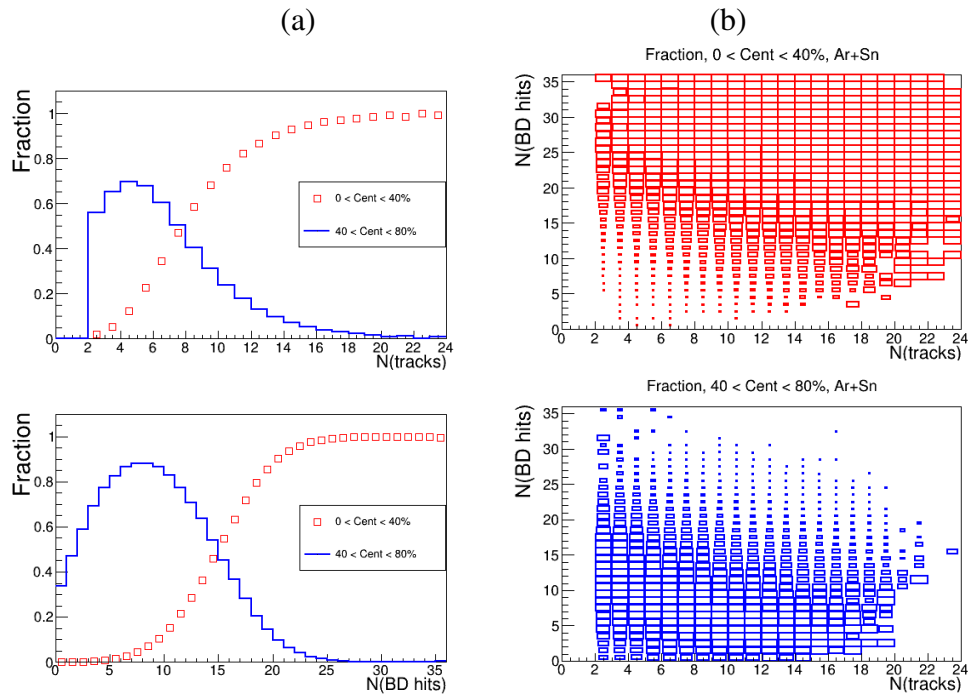


Figure 6: (a) Probability distribution of the number of tracks $N(\text{tracks})$ in the primary vertex (upper panel) and the number of hits $N(\text{BD})$ in the BD detector (lower panel) for events with centrality 0-40% (red open symbols) and 40-80% (blue histogram). (b) two-dimensional plot of the probability distribution of $N(\text{tracks})$ (horizontal axis) vs. $N(\text{BD})$ (vertical axis) in events with centrality 0-40% (upper panel) and 40-80% (lower panel).

232 The event centrality is determined as the fraction of the interaction cross section
 233 in the interval $[0, b]$ of the impact parameter b of the nucleus-nucleus collision
 234 to the total inelastic interaction cross section. Two classes of centrality: 1) 0-40%
 235 of the cross section (more central collisions) and 2) 40-80% of the cross section

236 (more peripheral collisions), are defined from the impact parameter distributions
 237 of Ar+A inelastic interactions simulated by the DCM-SMM model. The boundary
 238 impact parameters b_{40} and b_{80} for the definition of the two classes for interactions
 239 of Ar with various targets are given in Table 1. It was found that the number
 240 of tracks originating from the primary event vertex $N(\text{tracks})$ and the number of
 241 hits in the Barrel Detector $N(\text{BD})$ are anti-correlated with the impact parameter
 242 b . Using results of the DCM-SMM Monte Carlo simulation, the fractions of re-
 243 constructed events, which belong to the centrality classes 0-40% and 40-80%, are
 244 calculated. Fractions of events with centrality 0-40% and 40-80% are presented
 245 in Fig. 6 as functions of $N(\text{tracks})$, $N(\text{BD})$ and as a two-dimensional distribution
 246 $N(\text{tracks}) / N(\text{BD})$.

Table 1: The boundary impact parameters b_{40} and b_{80} for the definition of the two centrality classes 0-40% and 40-80%, and the inclusive inelastic cross section σ_{inel} for Ar+A interactions.

	Ar+C	Ar+Al	Ar+Cu	Ar+Sn	Ar+Pb
b_{40} , fm	4.23	4.86	5.66	6.32	7.10
b_{80} , fm	6.2	7.0	8.0	9.0	10.0
σ_{inel} , mb [36]	1470 ± 50	1860 ± 50	2480 ± 50	3140 ± 50	3940 ± 50

247 Fractions (probabilities) of events with centrality 0-40% and 40-80%, taken
 248 from the two-dimensional $N(\text{tracks}) / N(\text{BD})$ distributions are used as event weights
 249 to define the weighted number of reconstructed protons, deuterons and tritons in
 250 the y and p_T bins in data and simulation. The systematic uncertainty of the event
 251 centrality is estimated from the remaining difference in the shape of the $N(\text{tracks})$
 252 and $N(\text{BD})$ distributions in y and p_T bins in the simulation relative to the data.

6 Cross sections, multiplicities, and systematic uncertainties

The protons, deuterons and tritons in Ar+C, Al, Cu, Sn, Pb interactions are measured in the following kinematic ranges: transverse momentum $0.1 < p_T < 1.2$ GeV/c (protons), $0.15 < p_T < 1.45$ GeV/c (deuterons), $0.2 < p_T < 1.6$ GeV/c (tritons) and rapidity in the laboratory frame $0.9 < y < 2.5$ (protons), $0.7 < y < 2.3$ (deuterons), $0.7 < y < 2.1$ (tritons). The differential cross sections $d^2\sigma_{p,d,t}(y, p_T)/dydp_T$ and multiplicities $d^2N_{p,d,t}(y, p_T)/dydp_T$ of protons, deuterons and tritons produced in Ar+C, Al, Cu, Sn, Pb interactions are calculated using the relations:

$$d^2\sigma_{p,d,t}(y, p_T)/dydp_T = \Sigma[d^2n_{p,d,t}(y, p_T, N_{tr})/(\epsilon_{trig}(N_{tr})dydp_T)] \times 1/(L\epsilon_{p,d,t}^{rec}(y, p_T))$$

$$d^2N_{p,d,t}(y, p_T)/dydp_T = d^2\sigma_{p,d,t}(y, p_T)/(\sigma_{inel}dydp_T) \quad (1)$$

where the sum is performed over bins of the number of tracks in the primary vertex, N_{tr} , $n_{p,d,t}(y, p_T, N_{tr})$ is the number of reconstructed protons, deuterons and tritons in the intervals dy and dp_T , $\epsilon_{trig}(N_{tr})$ is the track-dependent trigger efficiency, $\epsilon_{p,d,t}^{rec}(y, p_T)$ is the reconstruction efficiency of protons, deuterons and tritons, L is the luminosity and σ_{inel} is the inelastic cross section for argon-nucleus interactions. The cross sections and multiplicities are evaluated for the two centrality classes: 0-40% and 40-80%.

Several sources are considered for the evaluation of the systematic uncertainty of the proton, deuteron and triton yield, $n_{p,d,t}$, and the reconstruction efficiency ϵ_{rec} . Some of them affect both the yield $n_{p,d,t}$ and the reconstruction efficiency, ϵ_{rec} . For these cases the correlated effect is taken into account by considering the variations on the $n_{p,d,t}/\epsilon_{rec}$ ratio. A detailed discussion of the systematic uncertainties associated with track reconstruction as well as with the trigger efficiency are given in ref. [8]. Additional sources specific to this analysis are listed below:

- Systematic uncertainty of the background subtraction in the mass-squared M^2 spectra of identified particles: it is estimated as the difference between the background integral under the p, d, t mass-squared windows taken from “mixed events” (as described in Section 3) and from the fitting of the M^2 spectra by a linear function. The latter is done in the M^2 range, excluding the proton, deuteron and triton signal windows.
- Systematic uncertainty calculated as half of the difference between the p/d/t yield measured in the ToF-400 and ToF-700 detectors in bins of rapidity y .

- Systematic uncertainty of the event centrality weights estimated 1) from the remaining difference in the shape of the N(track) and N(BD) distributions in y and p_T bins in the data and the simulation; 2) from the difference in the event centrality weights taken from the two-dimensional N(track) / N(BD) distribution relative to the one-dimensional N(BD) distribution.

Table 2 summarizes the mean values, averaged over p_T , y and N_{tr} of the systematic uncertainties of the various factors of Eq. (1), $n_{p,d,t}$, ϵ_{rec} , and ϵ_{trig} . The total systematic uncertainty from these sources, calculated as the square sum of their uncertainties from different sources, is listed in Table 2 for each target.

The luminosity is calculated from the beam flux Φ as given by the beam trigger (see Section 2) and the target thickness l using the relation: $L = \Phi\rho l$ where ρ is the target density expressed in atoms/cm³. The systematic uncertainty of the luminosity is estimated from the fraction of the beam that can miss the target, determined from the vertex positions, and found to be within 2%. The inelastic cross sections of Ar+C, Al, Cu, Sn, Pb interactions are taken from the predictions of the DCM-SMM model. The σ_{inel} uncertainties for Ar+C, Al, Cu, Sn, Pb interactions given in Table 1 are estimated from the empirical formulas taken from ref. [36,37].

Table 2: Mean systematic uncertainties averaged over the y , p_T ranges of protons, deuterons and tritons measured in argon-nucleus interactions.

	Ar+C %	Ar+Al %	Ar+Cu %	Ar+Sn %	Ar+Pb %
ϵ_{trig} p,d,t	9	7	7	7	7
protons					
n_p/ϵ_{rec}	15	6	8	14	11
Total	18	9	11	16	13
deuterons					
n_d/ϵ_{rec}	32	22	20	19	22
Total	33	23	21	20	23
tritons					
n_t/ϵ_{rec}	43	22	20	20	22
Total	44	23	21	21	23

304 7 Rapidity and mean transverse mass spectra

305 At a kinetic energy of 3.2 GeV/nucleon, the rapidity of the nucleon-nucleon center-
 306 of-mass (CM) system is $y_{CM} = 1.08$. The rapidity intervals covered in the present
 307 measurements, $0.9 < y < 2.5$, $0.7 < y < 2.3$ and $0.7 < y < 2.1$ for protons,
 308 deuterons and tritons, respectively, correspond therefore to the forward and central
 309 rapidity regions in the nucleon-nucleon CM system. The measured yields of
 310 protons, deuterons and tritons in m_T and y bins in the two centrality intervals in
 311 Ar+C,Al,Cu,Sn,Pb interactions can be found in ref. [38].

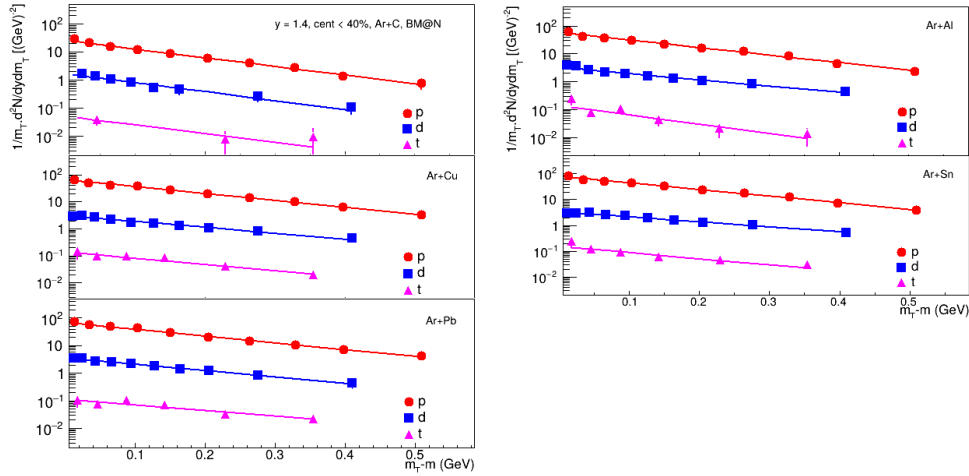


Figure 7: Invariant transverse mass spectra of protons, deuterons, tritons produced at rapidity $y = 1.4$ in Ar+C, Al, Cu, Sn, Pb interactions with centrality 0-40%. The vertical bars and boxes represent the statistical and systematic uncertainties, respectively. The lines show the results of the fit by an exponential function.

312 As an example, Fig. 7 shows the invariant transverse mass $m_T = \sqrt{m^2 + p_T^2}$
 313 spectra of protons, deuterons and tritons ($m = m_{p,d,t}$) produced in various targets
 314 at $y = 1.4$ in the 0-40% centrality class. The spectra are parameterised by an
 315 exponential function as:

$$\frac{1}{m_T} d^2N/dy dm_T = \frac{dN/dy}{T_0(T_0 + m)} \exp(-(m_T - m)/T_0) \quad (2)$$

316 where the fitting parameters are the integral of the m_T spectrum, dN/dy , and the
 317 inverse slope, T_0 . The dN/dy and T_0 values extracted from the fit can be found
 318 in ref. [38]. The dN/dy distributions of protons, deuterons and tritons produced

319 in collisions with centrality 0-40% in the various targets are shown in Figs. 8a, 9a
 320 and 10a, respectively. The figures show also the comparison of the results with
 321 predictions of the DCM-SMM and PHQMD models.

322 It is seen that the shapes of the particle rapidity density vary strongly with the
 323 target mass. For protons, the models have quite similar predictions, which are in
 324 reasonable agreement with the experimental results in the forward rapidity range.

325 Deuterons and tritons are predominately produced in the beam fragmentation
 326 region for Ar+C and Ar+Al interactions, whereas for heavier targets they are
 327 mostly produced at mid-rapidity. For deuterons and tritons, the models reason-
 328 ably describe the shape of the experimental spectra, but under-predict the absolute
 329 yields by a factor of about 5.

330 The dN/dy distributions of protons, deuterons and tritons produced in col-
 331 lisions with centrality 40-80% on the various targets are shown in Figs. 8b, 9b
 332 and 10b, respectively. The largest contribution is observed in the beam fragmen-
 333 tation region for all the targets. This tendency is reproduced by the DCM-SMM
 334 and PHQMD models, again the models under-estimate the absolute yields for
 335 deuterons and tritons by a factor of about 5. A significant deficit of deuterons
 336 and tritons in the PHQMD model relative to the experimental data has also been
 337 observed in central (0-10%) collisions of Au+Au at \sqrt{s} of 3 GeV by the STAR
 338 experiment [39].

339 The observed discrepancy between the data and the DCM-SMM and PHQMD
 340 models could be due to feed-down from excited nuclear states which are not taken
 341 into account in the models. At BM@N collision energies, the reaction zone con-
 342 sists of a hadronic gas dominated by nucleons and stable nuclei (d, t, He^3, He^4).
 343 However, in addition to these, there are many excited nuclear states with mass
 344 number $A \geq 4$. The role of the feeddown from these states for the description of
 345 light nuclei production in a broad energy range was discussed in ref. [40]. As
 346 reported in [40], feeding gives a significant contribution to the yields of d, t at
 347 NICA/BM@N energies: as much as 60% of all final tritons and 20% of deuterons
 348 may come from the decays of excited nuclear states.

349 The mean transverse kinetic energy, defined as $\langle E_T \rangle = \langle m_T \rangle - m$, is related to
 350 the T_0 value extracted from the fit of the m_T spectrum by the following equation:

$$\langle E_T \rangle = \langle m_T \rangle - m = T_0 + T_0^2 / (T_0 + m) \quad (3)$$

351 The $\langle E_T \rangle$ values of protons in the 0-40% centrality class are shown in Fig. 11a
 352 as a function of rapidity. The maximal values of $\langle E_T \rangle$ are measured at rapidity
 353 $1.0 < y < 1.3$, i.e. at mid-rapidity in the CM system. In general, the y dependence

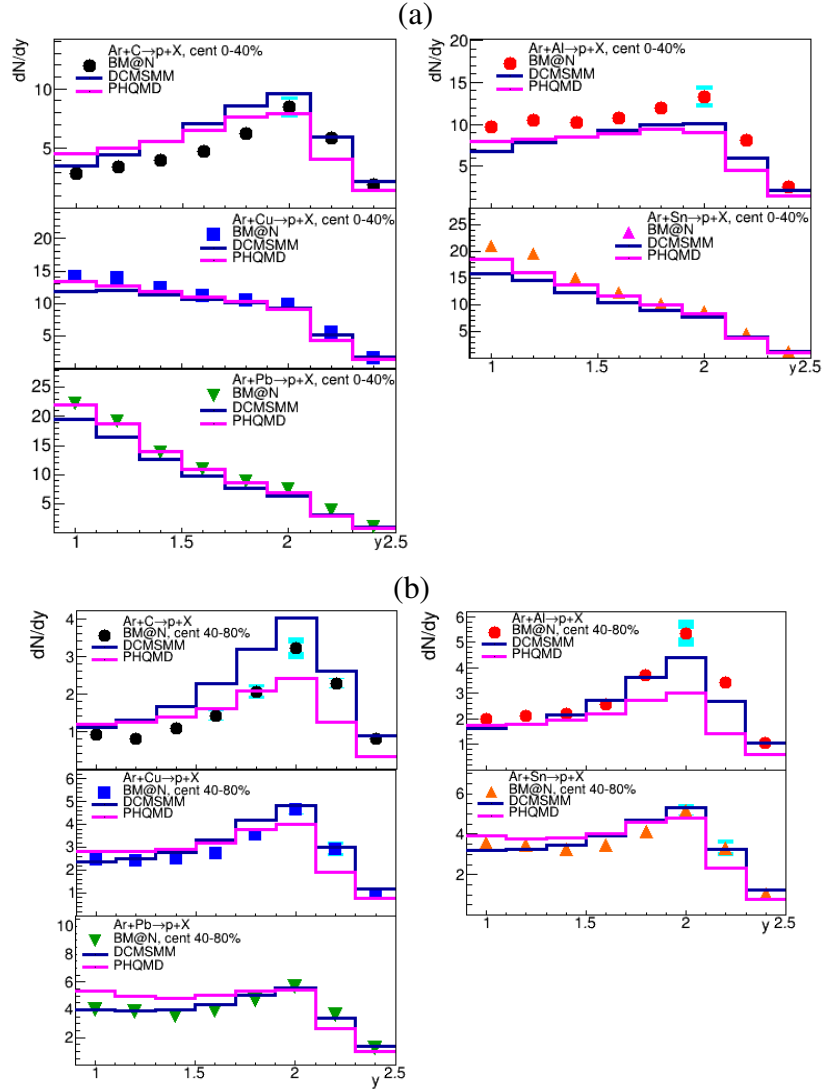


Figure 8: Rapidity distributions dN/dy of protons produced in Ar+C, Al, Cu, Sn, Pb interactions at 3.2A GeV with centrality 0-40% (a) and 40-80% (b). The results are integrated over p_T . The vertical bars and boxes represent the statistical and systematic uncertainties, respectively. The predictions of the DCM-SMM and PHQMD models are shown as blue and magenta lines.

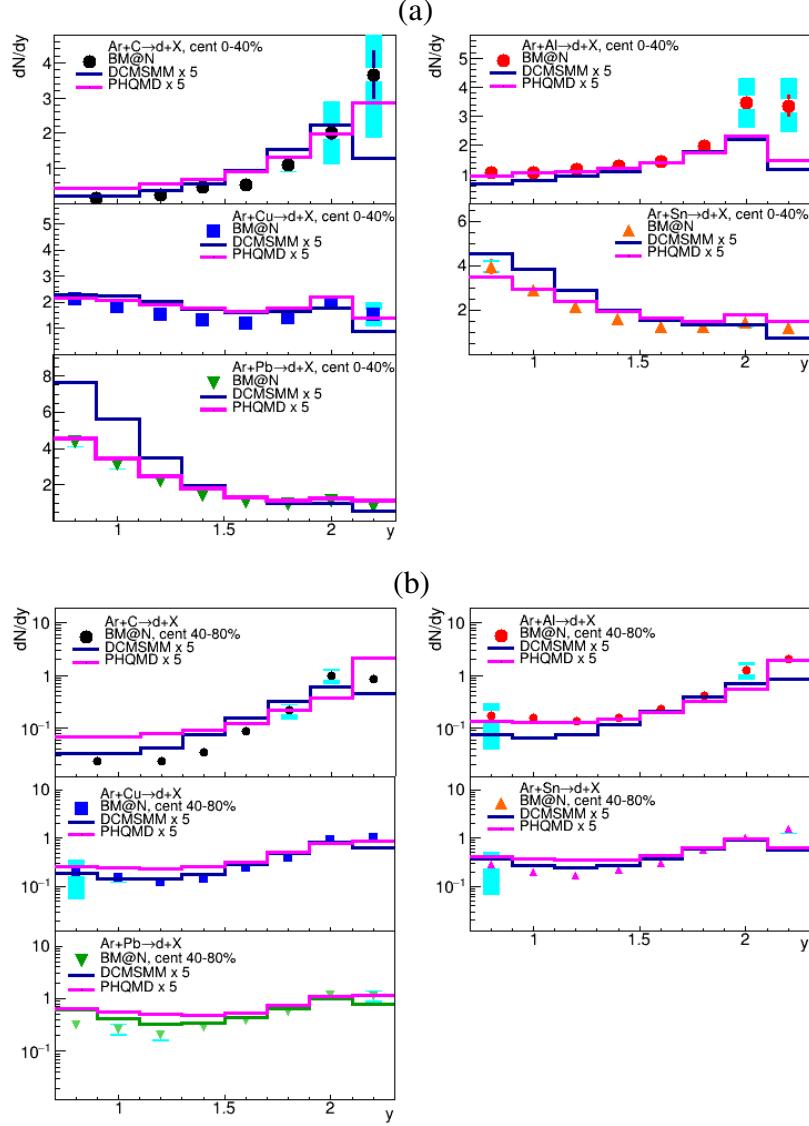


Figure 9: Rapidity distributions dN/dy of deuterons produced in Ar+C,Al, Cu, Sn, Pb interactions with centrality 0-40% (a) and 40-80% (b). The results are integrated over p_T . The vertical bars and boxes represent the statistical and systematic uncertainties, respectively. The predictions of the DCM-SMM and PHQMD models, multiplied by a factor 5, are shown as blue and magenta lines.

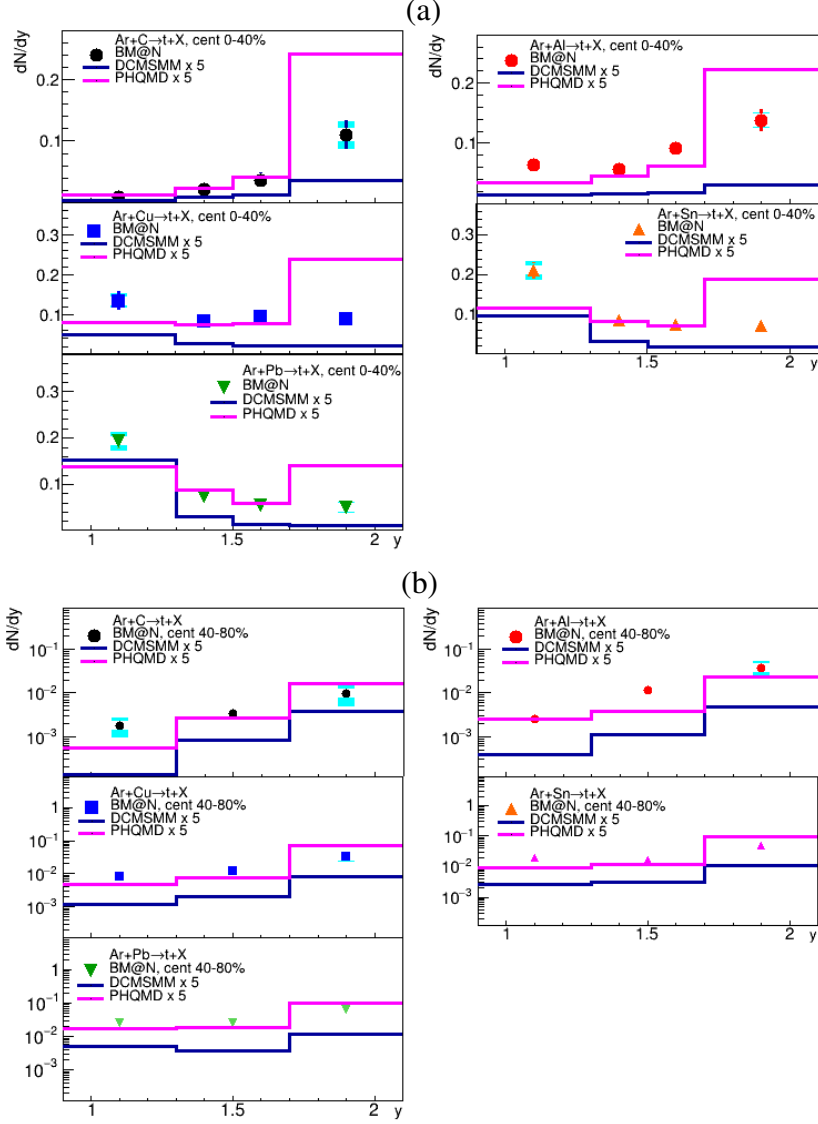


Figure 10: Rapidity distributions dN/dy of tritons produced in Ar+C,Al, Cu, Sn, Pb interactions with centrality 0-40% (a) and 40-80% (b). The results are integrated over p_T . The vertical bars and boxes represent the statistical and systematic uncertainties, respectively. The predictions of the DCM-SMM and PQHMD models, multiplied by a factor 5, are shown as blue and magenta lines.

354 of $\langle E_T \rangle$ for protons is consistent with predictions of the DCM-SMM and PHQMD
 355 models.

356 The $\langle E_T \rangle$ values for deuterons and tritons in the 0-40% centrality class are
 357 shown as functions of rapidity in Figs. 11b and 11c, respectively. PHQMD
 358 reproduces the rise of the data at mid-rapidity in CM for deuterons and tritons
 359 relative to protons, where as the DCM-SMM model predicts similar $\langle E_T \rangle$ values
 360 for protons, deuterons and tritons contrary to the experimental results.

361 A Blast-Wave model [47] was used to fit the invariant transverse mass spectra
 362 of protons, deuterons and tritons according to formula valid on the assumption
 363 of a box-like density profile with a uniform density inside the fireball (thermal
 364 source) region of transverse radius $r \leq R$:

$$\frac{d^2 N}{m_T dm_T dy} = \int_0^R m_T K_1 \left(\frac{m_T \cosh \rho(r)}{T} \right) I_0 \left(\frac{p_T \sinh \rho(r)}{T} \right) r dr \quad (4)$$

365 where I_0 and K_1 are the modified Bessel functions, T is the kinetic freeze-out
 366 temperature and $\rho(r) = \tanh^{-1} \beta(r)$ is the transverse radial flow rapidity pro-
 367 file. The transverse radial flow velocity $\beta(r)$ inside the fireball region is usually
 368 parametrized as $\beta = \beta_S (r/R)^n$, where β_S is the fireball-surface velocity. As-
 369 suming a linear velocity profile (exponent $n = 1$) one gets an average transverse
 370 radial flow velocity $\langle \beta \rangle = (2/3)\beta_S$. Fig. 12 shows the invariant m_T -spectra of
 371 p, d, t produced at rapidity $y = 1.4$ in Ar+Al,Cu,Sn,Pb interactions with centrality
 372 0-40%. The BM@N data are shown by symbols, the Blast-Wave model motivated
 373 fits are drawn by lines. The average radial flow velocity $\langle \beta \rangle$ and source temper-
 374 ature T at the kinetic freeze-out extracted from the Blast-Wave model fits to the
 375 transverse mass spectra of protons, deuterons and tritons measured in the range
 376 $0.9 < y < 1.5$ ($-0.18 < y^* < 0.42$) are given in Table 3. The quadratic sum
 377 of the statistical and systematical uncertainties of data points are used to evaluate
 378 the errors of the fit parameters. The parameters of the fit were assumed to be the
 379 same in the rapidity range of the fit. If a functional form of the Boltzmann approx-
 380 imation $T(0)/\cosh y^*$ with the midrapidity temperature $T(0)$ is used instead, the
 381 difference in the fit result is within 5%. One finds a flow velocity consistent with
 382 zero in central Ar+C collisions. Nuclear collisions of such small systems can be
 383 considered as a superposition of independent nucleon-nucleon interactions, there-
 384 fore, the density of participants reached in these reactions is probably not high
 385 enough to create a fireball with strong collective behavior. In contrast, for larger
 386 colliding systems (Ar+Al,Cu,Sn,Pb) the particle density and the re-scattering rate
 387 inside the reaction zone are higher, giving rise to a collective flow velocity. It ap-
 388 pears that the observed target mass dependence for T and $\langle \beta \rangle$ is weak at BM@N

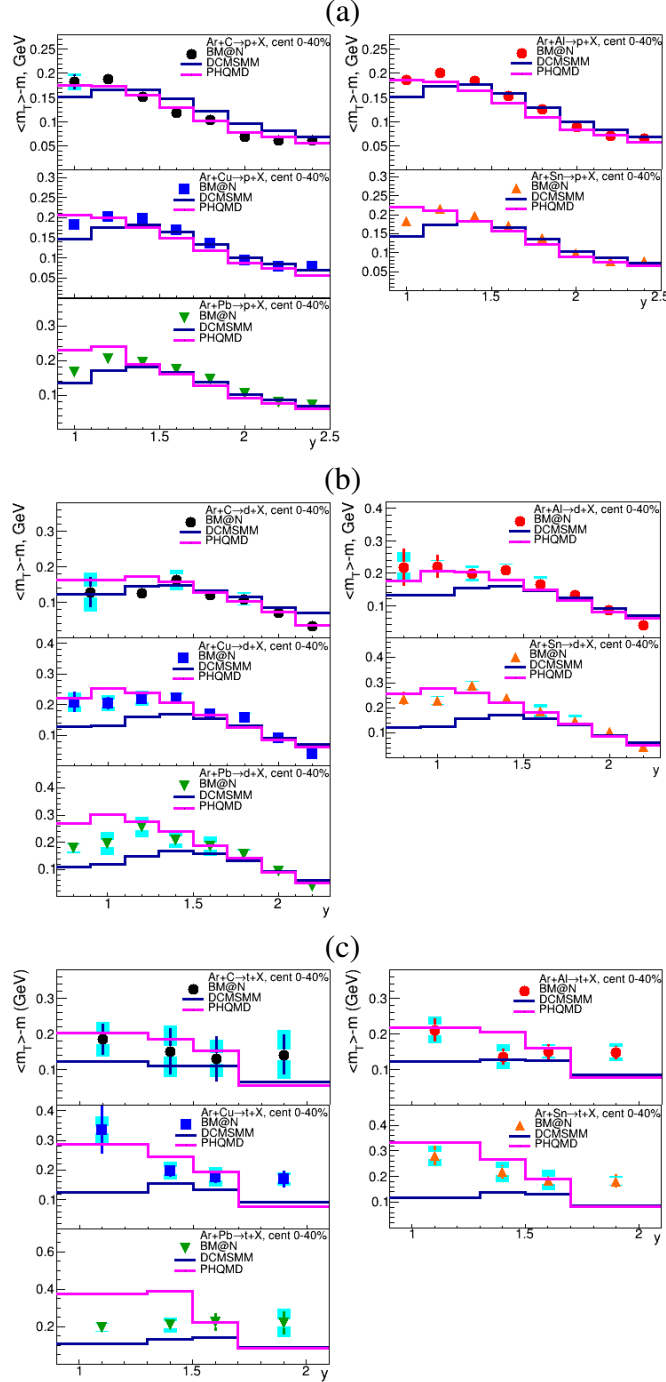


Figure 11: Rapidity y dependence of the mean transverse kinetic energy $\langle E_T \rangle = \langle m_T \rangle - m$ of protons (a), deuterons (b) and tritons (c) in Ar+C, Al, Cu, Sn, Pb interactions with centrality 0-40%. The vertical bars and boxes represent the statistical and systematic uncertainties, respectively. The predictions of the DCM-SMM and PHQMD models are shown as blue and magenta lines.

389 energies: fitted temperature and mean flow velocity are practically the same within
 390 the errors for studied colliding systems. This might be an indication that the in-
 391 crease of the reaction volume and the number of collisions with the target mass is
 not accompanied by a significant compression of the nuclear matter. The BM@N

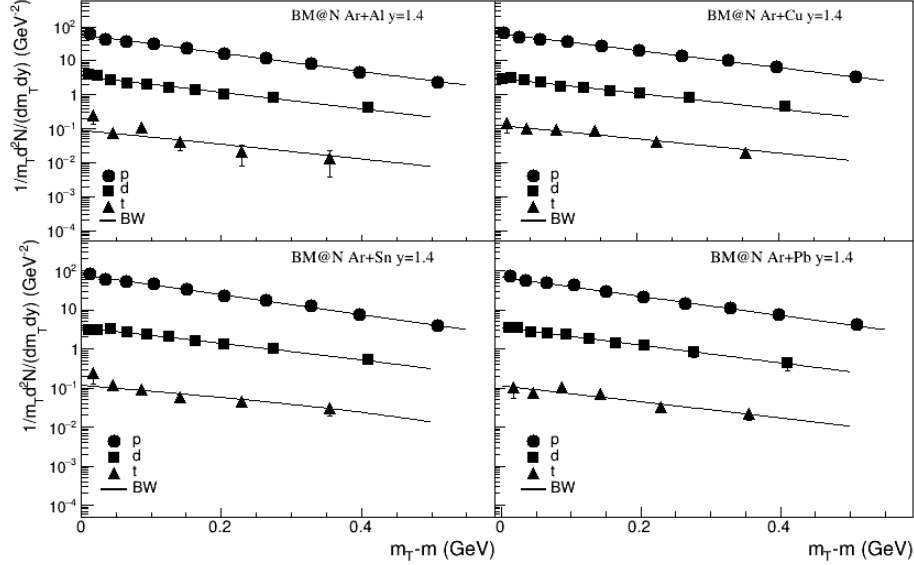


Figure 12: Invariant m_T -spectra of p, d, t produced at rapidity $y=1.4$ in Ar+Al,Cu,Sn,Pb interactions with centrality 0-40%. The BM@N data are shown by symbols, the Blast-Wave model motivated fits are drawn by lines.

392 transverse radial flow results could be compared with measurements at lower and
 393 higher energies. The FOPI experiment measured $\langle\beta\rangle \sim 0.35$ in Au+Au collisions
 394 at 1.2A GeV and found that the radial flow decreases below $\langle\beta\rangle \sim 0.20$ at
 395 lower energies and in interactions of middle-size nuclei [43]. Measurements of
 396 the EOS experiment [44] in Au+Au collisions at (0.25-1.15)A GeV are consistent
 397 with these results. At higher energies, the NA49 [42] ($\sqrt{s_{NN}}=6-17$ GeV)
 398 and STAR BES [45,46] ($\sqrt{s_{NN}}=7-39$ GeV) experiments measured $\langle\beta\rangle \sim 0.45$ in
 399 interactions of heavy nuclei (central Pb+Pb and Au+Au). The STAR experiment
 400 measured that the $\langle\beta\rangle$ values decrease with decreasing of the colliding system
 401 size [46]. The experiments also found that the temperature T increases from ~ 30
 402 MeV to ~ 120 MeV from energies of FOPI to NA49 and STAR BES. The $\langle\beta\rangle$
 403 and T values reported here in argon-nucleus interactions (except for Ar+C) are
 404 consistent with the energy and system size trends observed in these experiments.
 405

406 8 Coalescence factors

407 Within a coalescence model [18, 19, 21] nuclear fragment formation is character-
 408 ized by a coalescence factor B_A , defined through the invariant momentum spectra
 409 by the equation:

$$410 \quad E_A d^3 N_A / d^3 p_A = B_A (E_p d^3 N_p / d^3 p)^Z (E_n d^3 N_n / d^3 p)_{|p=p_A/A}^{A-Z},$$

411 where p_A and $p = p_A/A$ are momenta of the nuclear fragment **A** and the nu-
 412 cleon, respectively. It relates the yield N_A of nuclear fragments with charge Z
 413 and atomic mass number A to the yields of the coalescing nucleons N_p and N_n
 414 at the same velocity. Assuming that neutron momentum density is equal to the
 415 proton momentum density at freeze-out, the B_A value can be calculated as:

$$B_A = d^2 N_A / 2\pi p_{T,A} dp_{T,A} dy / (d^2 N_p / 2\pi p_T dp_T dy)^A / (n/p)^{A-Z}, \quad (6)$$

416 where n/p is the ratio of the numbers of produced neutrons to protons. The co-
 417 alescence factor is inversely related to the effective emission volume of the nu-
 418 cleons with nearby 3-momenta, increased due to finite size of the formed nuclear
 419 fragment [21]: $B_A \sim V_{eff}^{1-A}$. The strong position-momentum correlations present
 420 in the expanding source lead to a higher coalescence probability at larger values
 421 of p_T . Assuming a box-like transverse density profile of the source, the model
 422 predicts at small or moderate p_T [22]:

$$B_A \simeq g_s \Lambda_A A^{-1/2} C_A [(2\pi)^{3/2} / (m_T R_{||} (m_T) R_{\perp}^2 (m_T))]^{A-1} \exp[m_T (1/T_p - 1/T_A)], \quad (7)$$

Table 3: T and $\langle\beta\rangle$ values evaluated from the Blast-Wave fit of the transverse mass spectra of protons, deuterons and tritons produced in the rapidity range $-0.18 < y^* < 0.42$ in Ar+A interactions with centrality 0-40%. The errors represent the uncertainties of the fit to the data points with the quadratic sum of the statistical and systematical uncertainties.

	Ar+C	Ar+Al	Ar+Cu	Ar+Sn	Ar+Pb
T , MeV	140 ± 18	129 ± 10	132 ± 11	113 ± 10	126 ± 12
$\langle\beta\rangle$	0	0.19 ± 0.05	0.21 ± 0.04	0.27 ± 0.03	0.23 ± 0.05
χ^2/ndf	44/49	127/55	113/55	86/55	172/55

423 where $g_S = (2S + 1)/2^A$ is the spin factor of nuclear fragment A, Λ_A is a suppression
424 factor of correlated nucleons e.g due to a feed-down fraction of uncorrelated
425 nucleons produced in hyperon decays, C_A is a quantum correction factor related to
426 the finite fragment size [21,22], R_\perp and R_\parallel are the femtoscopic radii of the source
427 in the longitudinally co-moving system (LCMS) [22], T_p and T_A are the inverse
428 transverse momentum slopes for proton and fragment A, respectively. The Λ_A factor
429 is close to 1 in the BM@N energy range: fraction of nucleons originated from
430 hyperon decays is around 2% according to predictions of the UrQMD model [60].
431 The URQMD and PHQMD models yield in the BM@N rapidity range the n/p
432 ratio between 1.09 and 1.18, predicted for Ar+C and Ar+Pb interactions, respectively
433 (see also section 9).

434 Figs. 13a and 13b show the B_2 and B_3 values as functions of the transverse
435 momentum measured in argon-nucleus interactions with centrality 0-40%. The
436 transverse momentum is scaled to the atomic number of the nuclear fragment
437 (deuteron, triton), p_T/A . The yields of protons (N_p), deuterons (N_d) and tritons
438 (N_t) are measured in the same rapidity range, namely $0.9 < y < 1.7$ ($-0.18 <$
439 $y^* < 0.62$). The statistics of tritons is not sufficient to present B_3 for Ar+C
440 interactions. It is found, that B_2 and B_3 rise with p_T for all the measured targets.
441 The B_2 and B_3 values at low p_T are smaller for heavier targets compared to lighter
442 targets.

443 In order to compare the present measurements of B_2 and B_3 with previously
444 obtained results, the $B_2(p_T)$ and $B_3(p_T)$ values given in Figs. 13a and 13b are
445 extrapolated down to $p_T = 0$ using exponential fits of the form $b \exp[a(m_T -$
446 $m_A)]$ as predicted by the coalescence model model with a box-like density profile
447 [22](see equation 7). The fits are performed for the first four data points in the
448 range $p_T/A < 0.32$. The results of the extrapolation are given in Table 4.

449 The present results are compared in Fig.14a,b with the measurements of other
450 experiments [39,42,51–57]. The B_2 and B_3 results for Ar+A interactions with
451 centrality 0-40% are consistent with the energy dependence of the B_2 and B_3
452 factors for central interactions of heavy nuclei. It can be seen, that the BM@N
453 measurements follow the general trend of decreasing B_2 and B_3 values with rising
454 collision energy. The B_2 and B_3 values are inversely related to the coalescence
455 radius R_{coal} which is closely related to the LCMS femtoscopic radii of the source
456 $R_{out}, R_{side}, R_{long} = R_\parallel$ with $R_{out}(p_T = 0) = R_{side}(p_T = 0) = R_\perp$ [22]. Based
457 on equation 7 at $p_T = 0$, one can define $R_{coal} = \sqrt[3]{R_\parallel R_\perp^2}$ and calculate it from the
458 $B_2(p_T = 0)$ and $B_3(p_T = 0)$ values of deuterons and tritons. In the calculations,
459 the C_d and C_t factors from [51] are scaled according to the mass of the colliding

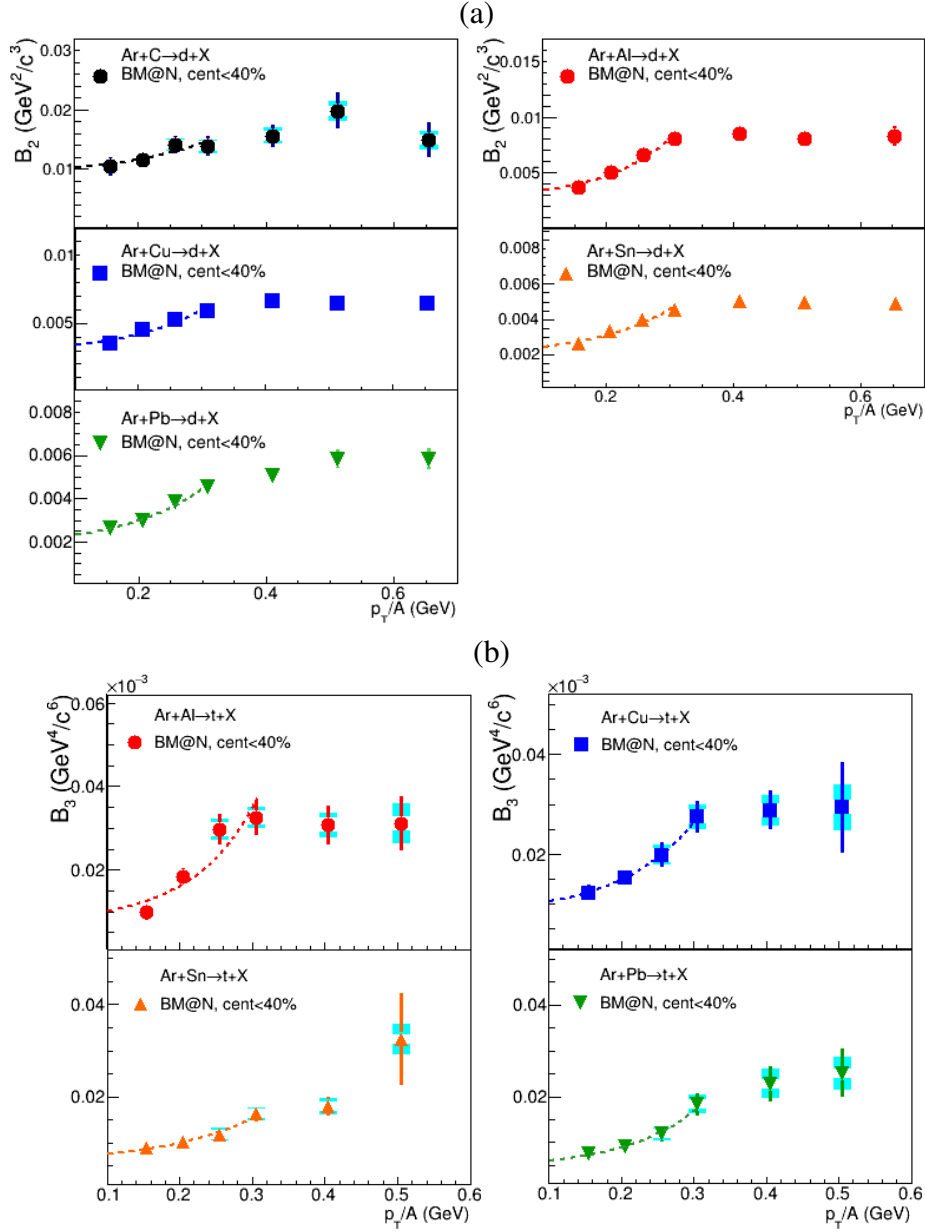


Figure 13: Coalescence parameter B_2 for deuterons (a) and B_3 for tritons (b) measured as a function of p_T/A in the rapidity range $-0.18 < y^* < 0.62$ in Ar+A collisions with centrality 0-40%. Dash lines show results of the fits in the range $p_T/A < 0.32$ described in the text.

Table 4: Coalescence parameters $B_2(p_T = 0)$ and $B_3(p_T = 0)$ extrapolated to $p_T = 0$ using an exponential fit to $B_2(p_T)$ and $B_3(p_T)$; coalescence radii $R_{coal}^d(p_T = 0)$ and $R_{coal}^t(p_T = 0)$ evaluated from the $B_2(p_T = 0)$ and $B_3(p_T = 0)$ values for deuterons and tritons produced in the rapidity ranges $-0.18 < y^* < 0.22$ and $0.22 < y^* < 0.62$ in Ar+A interactions with centrality 0-40%. The quoted errors are the quadratic sums of the statistical and systematic uncertainties.

	Ar+C	Ar+Al	Ar+Cu	Ar+Sn	Ar+Pb
$-0.18 < y^* < 0.22$					
$B_2(p_T = 0)/10^3, \text{GeV}^2/c^3$	6.4 ± 2.0	1.95 ± 0.7	2.6 ± 0.3	1.8 ± 0.2	1.35 ± 0.2
$B_3(p_T = 0)/10^6, \text{GeV}^3/c^4$		7.2 ± 2.2	5.8 ± 2.8	4.9 ± 0.6	2.6 ± 0.4
$R_{coal}^d(p_T = 0), \text{fm}$	1.8 ± 0.2	2.7 ± 0.3	2.5 ± 0.2	2.8 ± 0.2	3.1 ± 0.2
$R_{coal}^t(p_T = 0), \text{fm}$		2.4 ± 0.2	2.5 ± 0.2	2.5 ± 0.2	2.9 ± 0.2
$0.22 < y^* < 0.62$					
$B_2(p_T = 0)/10^3, \text{GeV}^2/c^3$	8.2 ± 2.0	3.56 ± 0.5	3.0 ± 0.8	2.06 ± 0.5	2.67 ± 0.4
$B_3(p_T = 0)/10^6, \text{GeV}^3/c^4$		9.6 ± 3.0	9.3 ± 2.9	7.3 ± 2.7	5.1 ± 2.3
$R_{coal}^d(p_T = 0), \text{fm}$	1.7 ± 0.2	2.2 ± 0.2	2.4 ± 0.2	2.7 ± 0.2	2.5 ± 0.2
$R_{coal}^t(p_T = 0), \text{fm}$		2.2 ± 0.2	2.3 ± 0.2	2.4 ± 0.2	2.5 ± 0.2

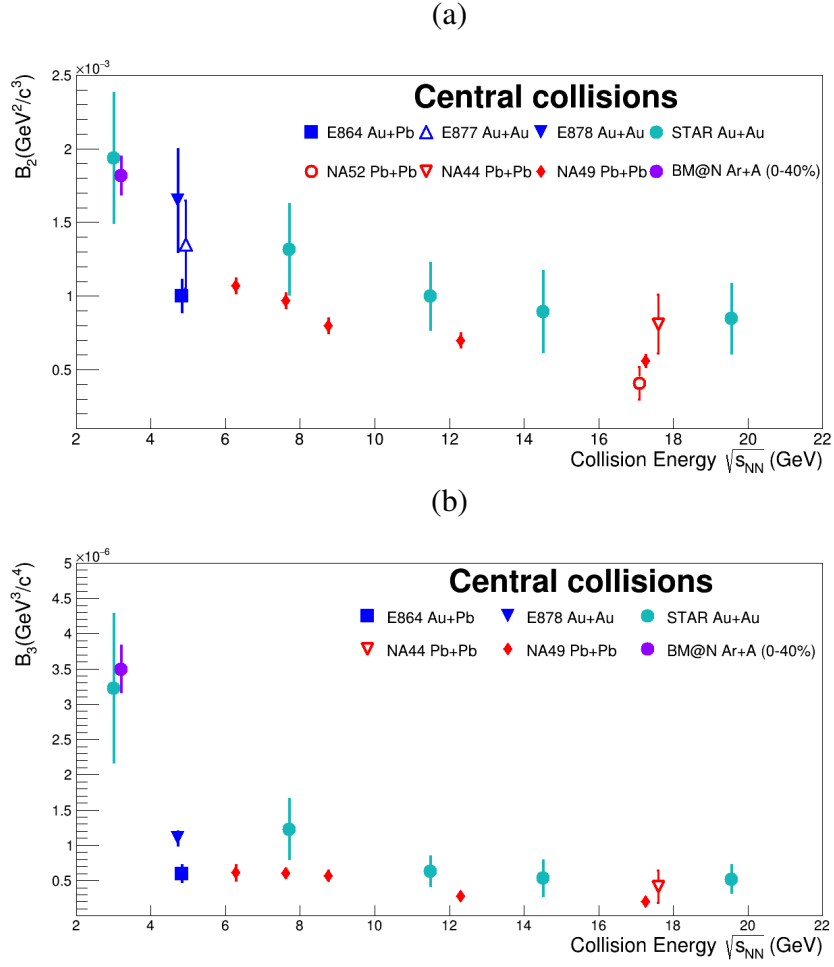


Figure 14: Coalescence parameters $B_2(p_T = 0)$ (a) and $B_3(p_T = 0)$ (b) for deuterons and tritons as a function of the nucleon-nucleon centre-of-mass energy. The BM@N result is a weighted average value calculated in the rapidity range $-0.18 < y^* < 0.22$ for Ar+Al,Cu,Sn,Pb interactions with centrality 0-40%.

460 systems to account for the suppression related to the increased effective volume
 461 due to the finite deuteron and triton radii (see Eq. (4.12) in [22]). The resulting
 462 values are in the range of 0.55-0.61 and 0.51-0.58 for C_d and C_t , respectively. The
 results for R_{coal} are given in Table 4.

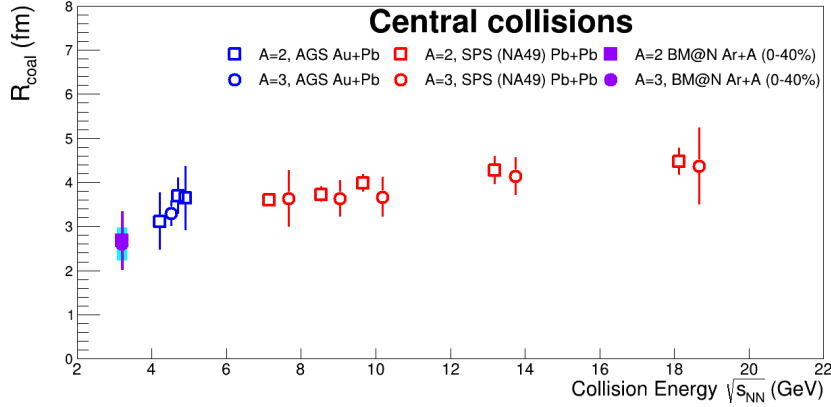


Figure 15: Coalescence radii R_{coal} for deuterons and tritons as a function of the nucleon-nucleon centre-of-mass energy. The BM@N result is a weighted average value calculated in the rapidity range $-0.18 < y^* < 0.22$ for Ar+Al,Cu,Sn,Pb interactions with centrality 0-40%.

463 The coalescence source radii for deuterons and tritons produced in Ar+Al,Cu,
 464 Sn,Pb interactions with centrality 0-40% are consistent within the errors. Their
 465 values are somewhat higher than for deuterons produced in Ar+C interactions.
 466 The BM@N values for the coalescence radii averaged for Ar+Al,Cu,Sn,Pb inter-
 467 actions are compared in Fig.15 with results at higher energies and larger collision
 468 systems as compiled in [42]. Figure 15 exhibits a weak increase of the coa-
 469 lescence radii as a function of the center-of-mass energy in the nucleon-nucleon
 470 system. Except for the carbon target, the BM@N results reported here are consis-
 471 tent with no or weak dependence of R_{coal} on target size within the experimen-
 472 tal uncertainties.
 473

474 **9 Baryon rapidity distributions, stopping and rapid-**
 475 **ity loss in Ar+A**

The total baryon number at given rapidity in Ar+A collisions at NICA/BM@N energies is basically determined by the nucleons and the light nuclei ($d, t, {}^3\text{He}$). According to the results on the rapidity spectra of protons and light nuclei, presented in Section 7, the number of nucleons bound in clusters contribute to the total number of baryons up to about 15% and 25% in central Ar+C and Ar+Pb reactions, respectively. To obtain the baryon rapidity distribution, we add up the baryon number of the measured protons, deuterons and tritons in every rapidity bin. The obtained distribution is then corrected for unmeasured baryons: neutrons, hyperons and ${}^3\text{He}$ nuclei. Calculations with the PHQMD and UrQMD models indicate that for all collision systems the n/p -ratio is of about 1.1 in the forward hemisphere varying slowly with rapidity and then increasing abruptly to ≈ 1.22 (the n/p -ratio in the projectile Ar-nucleus) at the beam rapidity. We use these model predictions to estimate the yield of neutrons n , furthermore, we assume that the $t/{}^3\text{He}$ ratio is equal to n/p . Hyperons contribute less than 2% to the total baryon number according to the PHQMD and UrQMD [60] models and are thus neglected. The total number of baryons B in a rapidity bin is then calculated as

$$B = p + n + 2.0 \cdot d + 5.7 \cdot t,$$

476 where the coefficient in front of t is $5.7 = 3.0$ (for tritons) + $3.0/1.1$ (for ${}^3\text{He}$).

477 The resulting baryon rapidity distributions for Ar+Cu collisions are shown in
 478 Fig. 16 as a function of the center-of-mass rapidity y^* : the left panel shows the
 479 results for 0-40% central collisions, and the right one is for 40-80% central col-
 480 lisions. As one can see from a dramatic difference in the shapes of the dn/dy
 481 distributions, more baryons are transported to midrapidity in the more central col-
 482 lisions. To describe those shapes, we fitted the measurements to a 3^{rd} order poly-
 483 nomial in y^{*2} (as suggested in ref. [58]), and the fit results are shown in Fig. 16 by
 484 solid curves.

485 The average rapidity loss is calculated as (below $y = y^*$)

$$\langle \delta y \rangle = y_b - \langle y \rangle, \quad (8)$$

486 where $y_b = 1.08$ is the rapidity of the projectile in the center-of-mass system, and

$$\langle y \rangle = \int_0^{y_b} y \frac{dn}{dy} dy \bigg/ \int_0^{y_b} \frac{dn}{dy} dy \quad (9)$$

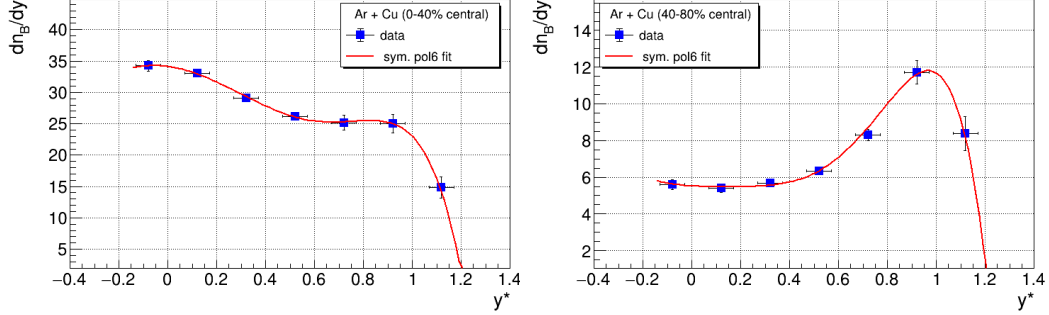


Figure 16: Left: Rapidity distribution of baryons in 0-40% central Ar+Cu collisions. The measurements are shown by solid dots, whereas the solid line is the results of a fit to a 3rd order polynomial in y^{*2} . Right: same for 40-80% central Ar+Cu collisions.

Table 5: The average rapidity loss $\langle \delta y \rangle$ in Ar+A reactions. The quoted uncertainties are statistical errors.

	Ar+C	Ar+Al	Ar+Cu	Ar+Sn	Ar+Pb
0-40%	0.42 ± 0.04	0.50 ± 0.03	0.58 ± 0.02	0.63 ± 0.02	0.65 ± 0.02
40-80%	0.38 ± 0.04	0.41 ± 0.04	0.45 ± 0.03	0.47 ± 0.03	0.48 ± 0.04

487 This equation refers to net-baryons, i.e. baryons minus antibaryons. At NICA
 488 energies, however, the production of antibaryons is so small that the difference
 489 between baryons and net-baryons is negligible.

490 The final $\langle \delta y \rangle$ values for central and peripheral collisions are listed in Table 5.
 491 A clear trend is observed: $\langle \delta y \rangle$ increases with the target mass and with central-
 492 ity. This behavior is expected because the probability of multiple interactions in
 493 the projectile-target overlap region also rises with centrality and target mass. The
 494 quoted uncertainties (statistical errors) are the standard errors of the mean $\langle y \rangle$
 495 calculated from the data points within the rapidity range $[0 - y_b]$. The systematic
 496 error in the rapidity loss values come from the uncertainty in the fitting procedure
 497 used to describe the baryon rapidity spectra. This uncertainty is taken as the dif-
 498 ference between the total baryon number estimated from the fit function and the
 499 one obtained from data points. It varies from 7% to 12%.

500 Figure 17 shows the energy dependence of the scaled average rapidity shift
 501 $\langle \delta y \rangle / y_b$ in nucleus-nucleus collisions as a function of $\sqrt{s_{NN}}$. The average of the
 502 BM@N results obtained in Ar+Al and Ar+Cu collisions is shown together with
 503 results from medium-size almost symmetric colliding systems from [59, 61, 62]

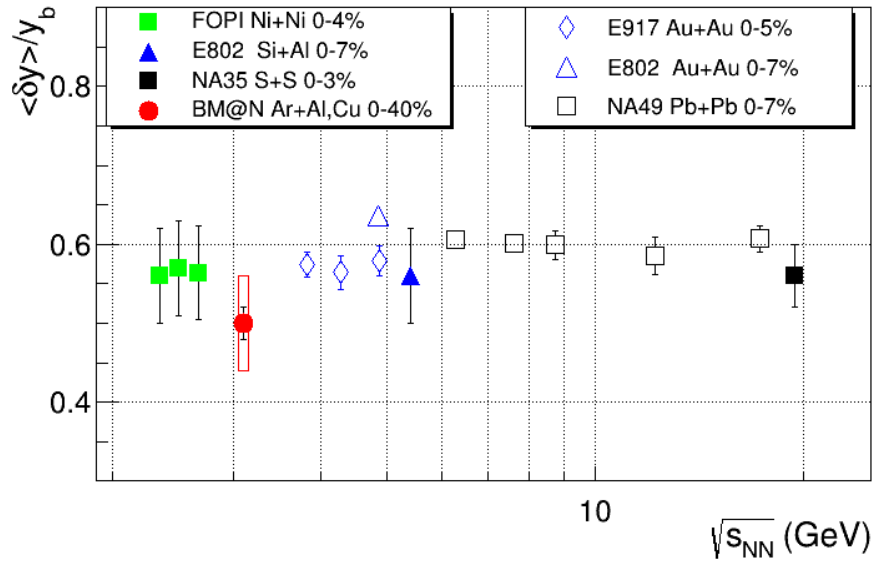


Figure 17: The excitation function of the scaled average rapidity loss $\langle \delta y \rangle / y_b$ in nucleus-nucleus collisions. Medium-size colliding systems [59, 61, 62] are drawn by solid symbols, while heavy systems [59, 63, 64] are shown by open ones. Centrality intervals are indicated in the legends. The BM@N data point is the average of Ar+Al and Ar+Cu results, the systematic error is shown by the box.

504 (solid symbols) and those from heavy colliding systems [59, 63, 64] (open sym-
 505 bols). The corresponding centrality intervals are indicated in the legends. As one
 506 can see, the scaled rapidity loss does not vary over a broad energy range.

507 10 Particle ratios

508 The rapidity and centrality dependence of the deuteron-to-proton ratio R_{dp}
 509 in Ar+A collisions at 3.2A GeV ($\sqrt{s_{NN}} = 3.1$ GeV) is presented in Fig. 18, a)-
 510 e). 0-40% central and 40-80% central collisions are shown by solid and open
 511 symbols, respectively. As one can see, R_{dp} rises strongly from midrapidity to the
 512 beam rapidity in more peripheral collisions. The same trend is observed in 0-40%
 513 central Ar+C collisions. In contrast, in 0-40% central collisions of argon nuclei
 514 with aluminum or heavier targets, R_{dp} indicates a plateau-like behavior
 515 near midrapidity followed by an increase toward the beam rapidity region. The
 516 plateau region for R_{dp} increases gradually with the target mass number covering
 517 almost all the measured rapidity range in Ar+Pb collisions.

518 The midrapidity R_{dp} values from central and peripheral Ar+A collisions as
 519 a function of the midrapidity baryon density dn_B/dy (obtained from the fits of
 520 Fig. 16) are presented in Fig. 18, f). As one can see, R_{dp} increases steadily for
 521 small values of dn_B/dy and then levels off at higher values.

522 For a system in chemical equilibrium and the size of the emitting source
 523 substantially larger than the deuteron radius, the ratio of the invariant yield of
 524 deuterons to the one of protons can be related to the average proton phase-space
 525 density at the freezeout $\langle f_p \rangle$ as

$$\langle f_p \rangle = \frac{R_{pn}}{3} \frac{E_d \frac{d^3 N_d}{d^3 P}}{E_p \frac{d^3 N_p}{d^3 p}} \quad (10)$$

526 where R_{pn} is the proton-to-neutron ratio, $P = 2p$, and the factor of 3 accounts
 527 for the spins of the particles [13]. The $\langle f_p \rangle$ value depends on the strength of nu-
 528 clear stopping in the reaction as well as on the outward flow effects. Figure 19
 529 (left panel) shows the evolution of the average proton's phase-space density as
 530 a function of transverse momentum. Here, the ratio of deuterons to protons is
 531 obtained in the rapidity range $0.02 < y^* < 0.42$ and at three p_T/A values: 0.15,
 532 0.3, and 0.45 GeV/c; the $\langle f_p \rangle$ values are calculated according to Eq. 10. The
 533 values of the R_{pn} ratio in the chosen phase-space region were taken from the
 534 UrQMD model. As one can see, $\langle f_p \rangle$ decreases with p_T in all reaction systems.

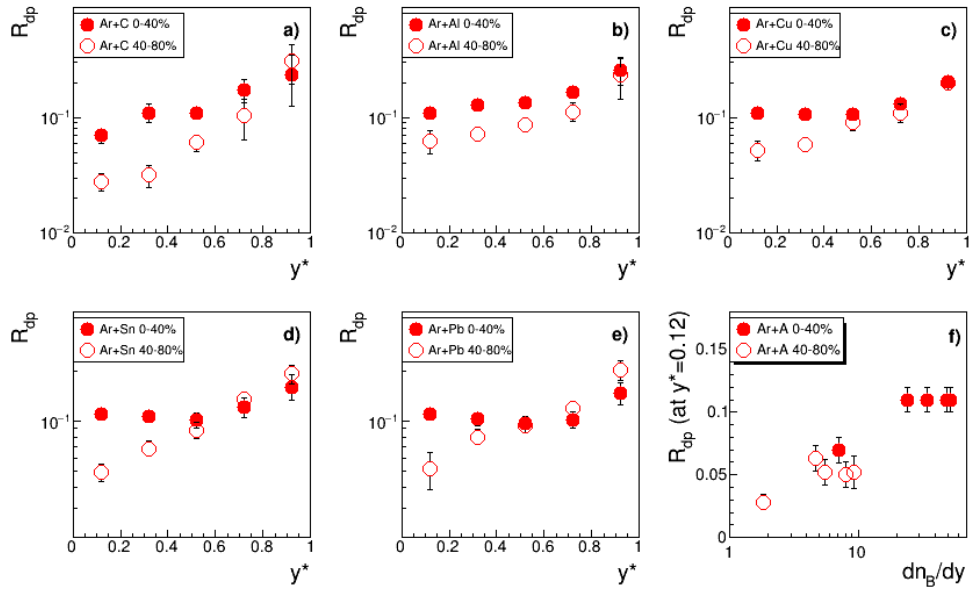


Figure 18: R_{dp} as a function of center-of-mass rapidity y^* in Ar+C (a), Ar+Al (b), Ar+Cu (c), Ar+Sn (d), and Ar+Pb (e) collisions. Central and peripheral collisions are shown by solid and open symbols, respectively. f): Midrapidity R_{dp} as a function of midrapidity baryon density dn_B/dy in Ar+A collisions.

535 Such a trend is indeed expected for a thermal source at a low phase-space density
 536 ($f \ll 1$) where $\langle f_p \rangle$ follows a Boltzmann distribution and decreases expo-
 537 nentially with p_T [65]. Two dashed lines in Fig. 19 show fits to an exponential
 538 function $const \cdot \exp(-p_T/p_{T0})$ for $\langle f_p \rangle$ from Ar+C and Ar+Pb reactions (p_{T0} is
 539 the slope parameter). It is known that the presence of outward flow in the sys-
 540 tem makes $f(p_T)$ flatter as the radial velocity increases [66]. The right panel of
 541 Fig. 19 shows the system size dependence of the slope parameter p_{T0} of the p_T -
 542 dependence for $\langle f_p \rangle$. Here the number of participants N_{part} for each reaction is
 543 taken as the average of the predictions of the UrQMD and DCM-SMM models.
 544 As one can see, the system size dependence is, indeed, correlated with the results
 545 on the radial velocity presented in Table 3: i.e. almost no radial expansion in
 546 Ar+C and approximately the same value of $\langle \beta \rangle$ in Ar+Al,Cu,Sn,Pb.

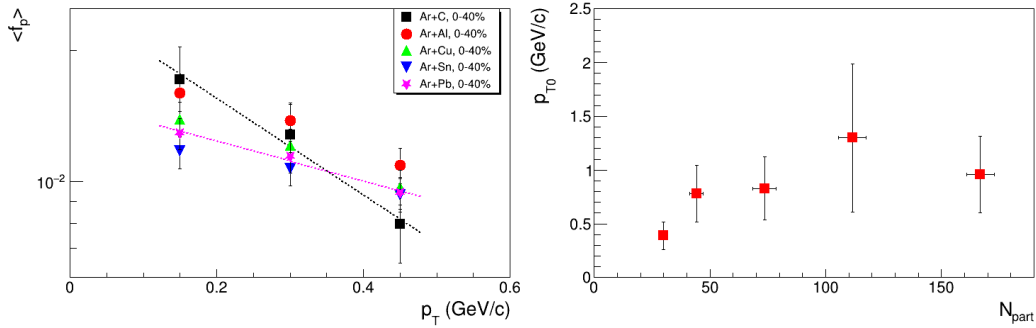


Figure 19: Left: Average proton phase-space density for 0-40% central Ar+A collisions as a function of p_T within the rapidity range $0.02 < y^* < 0.42$. Dashed lines show fits to exponent (see text for details). Right: The inverse slope parameter p_{T0} of the p_T -dependence of $\langle f_p \rangle$ as a function of N_{part} calculated for the C, Al, Cu, Sn and Pb targets from the UrQMD and DCM-SMM models.

547 It was identified long time ago that the nuclear cluster abundances and the
 548 entropy value attained in the collisions are related. According to early investiga-
 549 tions [67], in a mixture of nucleons and deuterons in thermal and chemical equilib-
 550 rium the entropy per nucleon S_N/A can be deduced from the deuteron-to-proton
 551 ratio R_{dp} as

$$\frac{S_N}{A} = 3.945 - \ln R_{dp} - \frac{1.25 R_{dp}}{1 + R_{dp}} \quad (11)$$

552 Furthermore, as the collision energy increases, the contribution of mesons S_π
 553 to the total entropy becomes important. Following [68], the entropy of pions per

554 nucleon can be estimated by

$$\frac{S_\pi}{A} = 4.1 \frac{N_\pi}{N_N}, \quad (12)$$

555 where $N_N = N_p + N_n$ is the total number of nucleons.

556 We thus calculated the total entropy S/A near midrapidity as the sum of the
 557 nucleon and pion entropy contributions according to Eq. 11 and Eq. 12. To es-
 558 timate S_π , we used the recently published BM@N results on positively charged
 559 pions [8], while the contribution of π^- , π^0 , and neutrons was obtained from the
 560 UrQMD model. We found that the contribution of pions to the total entropy does
 561 not exceed 25% in Ar+A collisions at NICA energies. Finally, S/A is found to be
 562 10.3, 7.8, 7.8, 7.9, and 7.9 in central Ar+C, Ar+Al, Ar+Cu, Ar+Sn, and Ar+Pb, re-
 563 spectively. The estimated uncertainty in S/A is about 15%. In Fig. 20 we present
 564 the energy dependence of S/A in central heavy-ion collisions. This compila-
 565 tion includes data from experiments that have published numerical values for the
 566 midrapidity yields of charged pions, protons, and light nuclei [42, 61, 69–73]. In
 567 this figure, we show the BM@N 'saturation' S/A -value of 8.0. As can be seen
 from the figure, the total entropy increases steadily with collision energy.

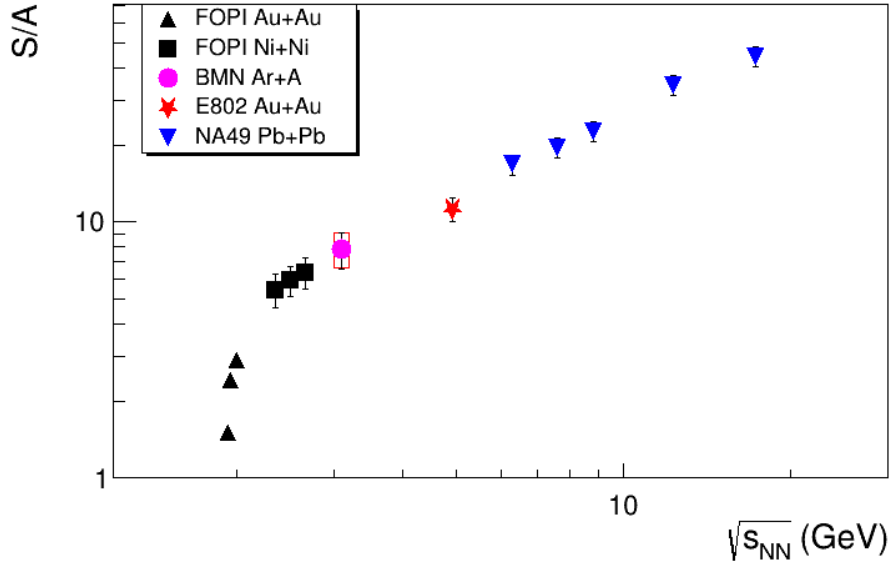


Figure 20: The excitation function of the entropy per baryon S/A from SIS/FOPI [61, 69], AGS/E802 [70], SPS/NA49 [42, 71–73] and NICA/BM@N (this study).

568

569 It has been established experimentally that the cluster production yields scaled
 570 by the spin degeneracy factor $(2J+1)$ decrease exponentially with the atomic mass
 571 number A [42, 74]. As an example, Fig. 21 (left panel) presents $dn/dy/(2J+1)$
 572 at midrapidity for p, d, t as a function of A from 0-40% central Ar+Sn collisions.
 573 The particle rapidity density values are extracted from the fits of Fig. 7. The A -
 574 dependence of the yields was fitted to a form:

$$\frac{dn}{dy}(A) = \text{const}/p^{A-1}, \quad (13)$$

575 where the parameter p ('penalty factor') determines the penalty of adding one
 576 extra nucleon to the system.

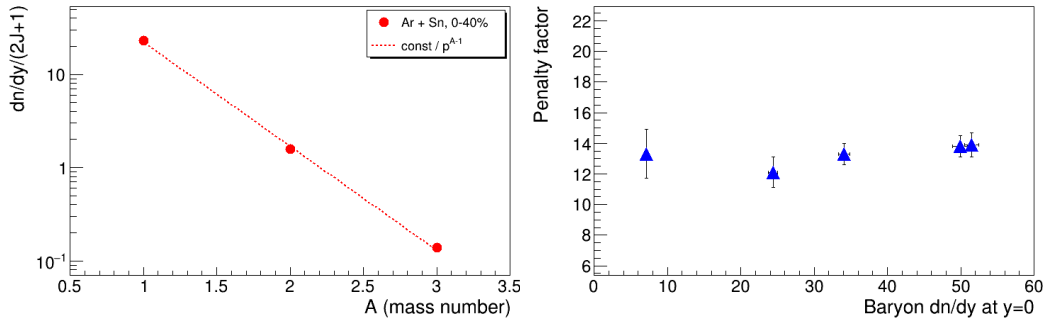


Figure 21: Left: Midrapidity $dn/dy/(2J+1)$ for p, d, t from central Ar+Sn collisions. The dashed line is a fit to Eq. 13. Right: Penalty factor from central Ar+A collisions versus baryon rapidity density at midrapidity.

577 The p -factors from central Ar+A collisions are listed in Table 6 and shown in
 578 Fig. 21 (right panel) as a function of the midrapidity baryon density. The quoted
 579 errors are the statistical ones obtained from the fit to Eq. 13.

580 In the framework of a statistical approach, the penalty factor is determined as:

$$p = e^{(m-\mu_B)/T}, \quad (14)$$

581 where μ_B, T , and m being the baryochemical potential, freezeout temperature,
 582 and nucleon mass, respectively [15]. Equation 14 can be used to determine the
 583 source thermodynamic freeze-out parameters T and μ_B as an alternative approach
 584 instead of the standard method based on the analysis of hadron abundances in the
 585 framework of a thermal statistical model [75]. As reported in ref. [76], the values
 586 of kinetic and chemical freeze-out temperatures are similar in heavy-ion collisions

Table 6: Penalty factor p , temperature T (from Table 3), and baryochemical potential μ_B in 0-40% central Ar+A collisions. The quoted uncertainty is the quadratic sum of the statistical and systematic errors.

Reaction	p	T (MeV)	μ_B (MeV)
Ar+C	13.6 ± 1.6	140.0 ± 18.0	575.7 ± 49.5
Ar+Al	12.1 ± 1.0	129.0 ± 10.0	616.4 ± 27.1
Ar+Cu	13.3 ± 0.7	132.0 ± 11.0	596.4 ± 29.3
Ar+Sn	13.8 ± 0.7	113.0 ± 10.0	641.4 ± 26.9
Ar+Pb	13.9 ± 0.8	126.0 ± 12.0	606.4 ± 32.4

587 below $\sqrt{s_{NN}} = 5$ GeV. Thus, we can use the value of T obtained in the analysis
 588 of transverse mass spectra of particles and listed in Table 3 as an estimate for a
 589 'universal' freeze-out temperature. From Eq. 14, one can write a formula for μ_B
 590 as

$$\mu_B = m - T \ln p \quad (15)$$

591 The resulting (T, μ_B) freeze-out parameters for central Ar+A collisions are
 592 tabulated in Table 6 and shown in Fig. 22 together with world data for central
 593 Au+Au and Pb+Pb collisions from ref. [75]. The BM@N results from medium-
 594 size Ar+A collisions are above the trend defined by world data for collisions of
 595 heavy ions (the dashed line shows the parameterization for heavy-ion data that is
 596 taken from ref. [75]). It may indicate that a weaker pressure gradient formed in
 597 collisions of medium-size nuclei results in a larger freezeout temperature compared
 598 to central collisions of heavy nuclei.

599 Recently, the STAR experiment reported measurements of the compound yield
 600 ratio $R_{ptd} = N_p N_t / N_d^2$ of protons (N_p) and tritons (N_t) to deuterons (N_d) [56].
 601 Coalescence models predict [77] that a non-monotonic behaviour of the ratio as a
 602 function of the system size or collision energy is a signature of the neutron density
 603 fluctuations Δn : $R_{ptd} \approx g(1 + \Delta n)$ with a color factor $g \simeq 0.29$. Following this
 604 argument, R_{ptd} is a promising observable to search for the critical point and/or a
 605 first-order phase transition in heavy-ion collisions [78]. In coalescence models,
 606 the compound yield ratio should increase as the size of the system decreases.
 607 Indeed, this effect is observed by the STAR experiment [57].

608 To evaluate the R_{ptd} ratio, mean values of the dN/dy distributions for protons,
 609 deuterons and tritons are calculated in two rapidity ranges: $0.9 < y < 1.3$
 610 ($-0.18 < y^* < 0.22$) and $1.3 < y < 1.7$ ($0.22 < y^* < 0.62$). The results are
 611 given in Table 7 for argon-nucleus interactions with centrality 0-40%. The quoted

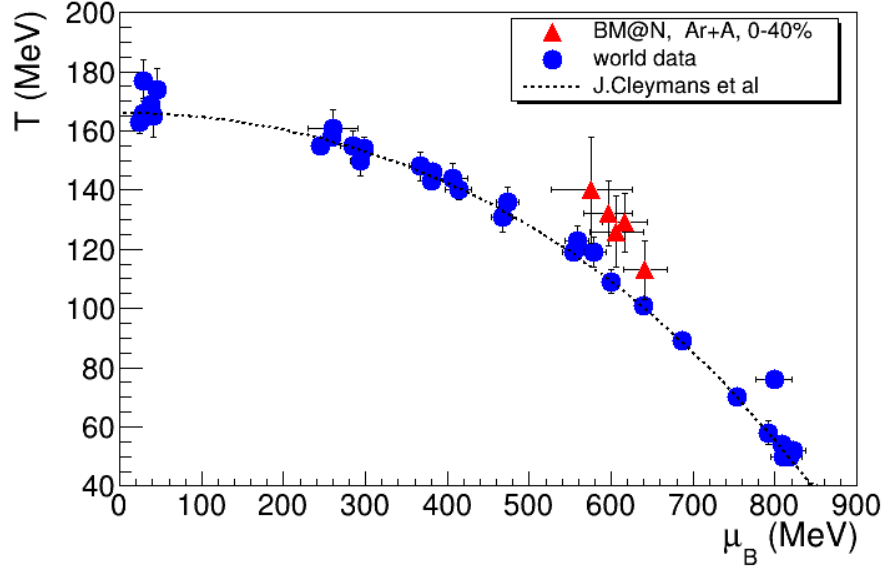


Figure 22: Freeze-out (T, μ_B) parameters for A+A collisions. BM@N results are from this study, world data and the parameterization for the freezeout line (dashed line) are from [75].

Table 7: $N_p N_t / N_d^2$ values evaluated from the mean dN/dy values of protons, deuterons and tritons over the rapidity range $-0.18 < y^* < 0.22$ and $0.22 < y^* < 0.62$ in Ar+A interactions with centrality 0-40%. The quoted errors are the quadratic sums of the statistical and systematic uncertainties.

	Ar+C	Ar+Al	Ar+Cu	Ar+Sn	Ar+Pb
$N_p N_t / N_d^2$ ($-0.18 < y^* < 0.22$)	0.52 ± 0.18	0.53 ± 0.10	0.66 ± 0.16	0.68 ± 0.12	0.57 ± 0.11
$N_p N_t / N_d^2$ ($0.22 < y^* < 0.62$)	-	0.40 ± 0.07	0.60 ± 0.08	0.50 ± 0.08	0.51 ± 0.12

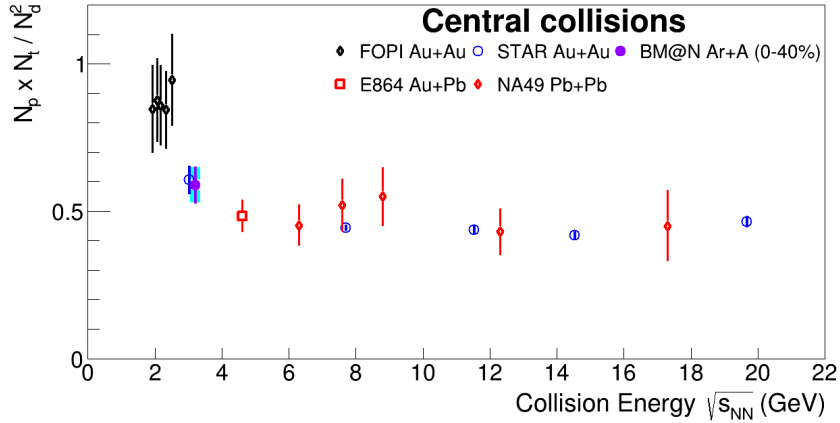


Figure 23: Compound yield ratio $N_p \cdot N_t / N_d^2$ of protons (N_p) and tritons (N_t) to deuterons (N_d^2) as a function of the centre-mass energy of nucleus-nucleus interactions. The BM@N result is the weighed average value in the rapidity range $-0.18 < y^* < 0.22$ calculated for Ar+Al,Cu,Sn,Pb interactions with centrality 0-40%.

612 error is the quadratic sum of the statistical and systematic uncertainties. No signif-
613 icant variation of the $N_p N_t / N_d^2$ values is observed with the various targets. Taking
614 the differences as a systematic uncertainty, the weighted average value of the compo-
615 und ratio is estimated to be 0.59 ± 0.06 for $-0.18 < y^* < 0.22$ and 0.46 ± 0.06
616 for $0.22 < y^* < 0.62$, where the uncertainty is the quadratic sum of the statistical
617 and systematic uncertainties. Within the uncertainties there is no strong depen-
618 dence of the R_{ptd} ratio on rapidity in the measured rapidity range. The BM@N
619 value for R_{ptd} for $-0.18 < y^* < 0.22$ is compared in Fig. 23 with the measure-
620 ments of other experiments. The BM@N result lays between the values of 0.8-1.0
621 derived by the FOPI experiment [43] at lower energies and the values of 0.4-0.5
622 obtained by the E864, STAR and NA49 experiments at higher CM energies \sqrt{s}
623 from 4.3 to 18 GeV [42, 52, 57, 79]. The BM@N value for R_{ptd} is consistent with
624 the STAR Au+Au result measured in the fixed target mode at \sqrt{s} of 3 GeV [39].

625 11 Summary

626 First results of the BM@N experiment are presented on the proton, deuteron and
627 triton yields and their ratios in argon-nucleus interactions at the beam kinetic en-

628 ergy of 3.2 AGeV. They are compared with the DCM-SMM and PHQMD models
629 and with previously published results of other experiments.

630 The transverse mass m_T spectra are measured and the mean transverse kinetic
631 energy $\langle E_T \rangle = \langle m_T \rangle - m$ are presented for more central 0-40% events as func-
632 tions of the rapidity y and mass m of the nuclear fragment. The $\langle E_T \rangle$ values
633 are found to depend linearly on the mass m . The source temperature at kinetic
634 freeze-out and the average radial velocity are extracted.

635 The rapidity density dN/dy of protons, deuterons and tritons are presented
636 for the whole p_T range in two centrality ranges. The DCM-SMM and PHQMD
637 models reproduce the shapes of the spectra, but underestimate the deuteron and
638 triton yields by a factor of about 5.

639 The average rapidity loss $\langle \delta y \rangle$ increases with the target mass and with the col-
640 lision centrality. In contrast, the rapidity loss scaled to the beam rapidity $\langle \delta y \rangle / y_b$
641 in almost symmetric heavy-ion collisions does not vary over a broad energy range.

642 The ratio of deuterons to protons R_{dp} rises in peripheral collisions and levels
643 off in central ones, possibly indicating a saturation of the nucleon phase-space
644 density at freezeout. The entropy per baryon S/A was estimated to be $S/A \approx 8$
645 nicely fitting in the trend of the S/A energy dependence established from other
646 experimental results.

647 The freezeout fireball parameters T obtained from the transverse mass spectra
648 and the baryo-chemical potential μ_B derived from a coalescence analysis were
649 found to follow the trend of the world T, μ_B values obtained from a statistical
650 analysis of particle abundances.

651 The deuteron to proton and triton to proton yield ratios are used to calculate
652 the coalescence parameters B_2 and B_3 for deuterons and tritons. The coalescence
653 radii of the deuteron and triton source are extracted from the B_2 and B_3 values
654 extrapolated to $p_T = 0$ and compared with results of other experiments.

655 The compound yield ratio $N_p N_t / N_d^2$ of protons and tritons to deuterons is
656 evaluated and compared with other measurements at lower and higher energies.
657 The results follow the general trend of decreasing values of B_2, B_3 and $N_p N_t / N_d^2$
658 ratio with increasing energy.

659 **Acknowledgments.** The BM@N Collaboration acknowledges the efforts of the
660 staff of the accelerator division of the Laboratory of High Energy Physics at JINR
661 that made this experiment possible. The BM@N Collaboration acknowledges
662 support of the HybriLIT of JINR for the provided computational resources.

References

- 663
- 664 [1] B. Friman, W. Nörenberg, and V.D. Toneev, Eur. Phys. J. A 3 (1998).
- 665 [2] J. Randrup and J. Cleymans, Phys. Rev. C 74 (2006) 047901.
- 666 [3] Ch. Fuchs, Prog. Part. Nucl. Phys. 56 (2006) 1-103.
- 667 [4] NICA White Paper, Eur. Phys. J. A 52 (2016).
- 668 [5] BM@N Conceptual Design Report: http://nica.jinr.ru/files/BM@N/BMN_CDR.pdf
- 669
- 670 [6] M. Kapishin (for the BM@N Collaboration), Nucl. Phys. A 982 (2019) 967-
- 671 970.
- 672 [7] M. Kapishin (for the BM@N Collaboration), SQM 2019 proceedings, 285
- 673 Springer Proc. Phys. 250 (2020) 21-27.
- 674 [8] S.Afanasiev et al. (BM@N Collaboration), JHEP 07 (2023) 174.
- 675 [9] W. Busza and A. S. Goldhaber, Phys. Lett. 139B, 235 (1984).
- 676 [10] G.C. Rossi and G. Veneziano, Phys. Rep. 63 (1980) 153.
- 677 [11] A. Capella and B. Z. Kopeliovich, Phys. Lett. B 381, 325 (1996)
- 678 [12] D. Kharzeev, Phys. Lett. B 378, 238 (1996)
- 679 [13] M.Murray and B. Holzer, Phys Rev. C 63, 054901 (2000).
- 680 [14] A. Andronic, P. Braun-Munzinger, and J. Stachel, Phys. Lett. B 673, 142
- 681 (2009).
- 682 [15] T.A. Armstrong et al (E864 Collaboration) Phys. Rev. Lett. 83, 5431 (1999).
- 683 [16] G. Bertsch and J. Cugnon, Phys. Rev. C 24, 2514 (1981).
- 684 [17] J. I. Kapusta, Phys. Rev. C 24, 2545 (1981).
- 685 [18] S.T. Butler and C.A. Pearson, Phys. Rev. 129, 836 (1963).
- 686 [19] A. Schwarzschild and C. Zupancic, Phys. Rev. 129, 854 (1963).

- 687 [20] S. Mrowczynski, Phys. Lett. B 277, 43 (1992).
- 688 [21] H. Sato, K. Yazaki, Phys. Lett. 98B (1981) 153
- 689 [22] R. Scheibl and U. Heinz, Phys. Rev. C 59, 1585 (1999).
- 690 [23] N. Amelin, K. Gudima, and V. Toneev, Sov. J. Nucl. Phys. 51, 1093 (1990).
- 691 [24] M. Baznat, A. Botvina, G. Musulmanbekov, V. Toneev, V. Zhezher, Phys.
692 Part. Nucl. Lett. 17 (2020) no. 3; arXiv: 1912.09277v.
- 693 [25] J.Aichelin, E. Bratkovskaya et al, Phys. Rev. C 101, 044905 (2020)
- 694 [26] BM@N project:
695 https://bmn.jinr.int/detector/project/BMN_project.pdf
- 696 [27] S. Afanasiev et al., arXiv:2312.17573 [hep-ex]
- 697 [28] D. Baranov et al., JINST 12 (2017) no. 06, C06041
- 698 [29] V. Babkin et al., Nucl. Instrum. Meth. A 824, P.490-492 (2016); V. Babkin
699 et al., Proceedings of Science, 2014, Vol.213 (Proceedings of TIPP-2014),
700 P.289.
- 701 [30] N. Kuzmin et al., Nucl. Instrum. Meth. A 916, P. 190-194 (2019).
- 702 [31] K. Alishina et al., Phys. Part. Nucl., 53 (2022) no. 2, 470-475.
- 703 [32] V. Akishina and I. Kisel, J. Phys.: Conf. Ser. 599, 012024 (2015), I. Kisel,
704 Nucl. Instrum. Meth. A 566, 85 (2006).
- 705 [33] CERN Program Library, Long Writeup W5013, Geneva, CERN, 1993.
- 706 [34] <https://git.jinr.ru/nica/bmnroot>
- 707 [35] V.Plotnikov, L.Kovachev, A.Zinchenko, Phys. Part. Nuclei Lett. 20 (2023),
708 1392–1402
- 709 [36] K.Kanaki, PhD Thesis, Technische Universität Dresden, 2007.
- 710 [37] H.Angelov et al., P1-80-473, JINR, Dubna.

- 711 [38] BM@N web-page:
712 https://bmn.jinr.int/wp-content/uploads/2024/07/PiKpaper_TabRes_v3.pdf
- 713 [39] M.I.Abdulhamid et al. (STAR Collaboration), [nucl-ex] arXiv:2311.11020
- 714 [40] V.Vovchenko et al, Phys. Lett. B 809 (2020) 135746
- 715 [41] D.R.Tilley, H.R. Weller, G.M. Hale, Nucl. Phys. A 541 (1992) 1
- 716 [42] T.Anticic et al. (NA49 Collaboration) Phys. Rev. C 94, 044906 (2016)
- 717 [43] W.Reisdorf et al. (FOPI Collaboration) Nucl.Phys.A 848 (2010) 366-427
- 718 [44] M.A.Lisa et al. (EOS Collaboration) Phys.Rev.Lett.75 (1995) 2662
- 719 [45] L.Kumar (for the STAR Collaboration), Nucl. Phys. A 931, 1114 (2014)
- 720 [46] L.Adamczyk et al. (STAR Collaboration) Phys.Rev.C 96 (2017) 4, 044904
- 721 [47] E.Schnedermann, J.Sollfrank, and U.W.Heinz, Phys.Rev.C 48 (1993) 2462.
- 722 [48] A.Z.Mekjian, Phys. Rev. Lett. 38, 640 (1977); Phys. Rev. C 17, 1051 (1978);
723 and Nucl. Phys. A 312, 491 (1978).
- 724 [49] J.I.Kapusta, Phys. Rev. C 21, 1301 (1980).
- 725 [50] PDG group review, J. Phys. G 37, 075021 (2010), Introduction, section 5.2
- 726 [51] I.G.Bearden et al. (NA44 Collaboration), Eur. Phys. J. C 23, 237–247 (2002).
- 727 [52] T.A.Armstrong et al. (E864 Collaboration), Phys. Rev. C 61, 064908 (2000),
728 nucl-ex/0003009
- 729 [53] J.Barrette et al. (E877 Collaboration), Phys. Rev. C 61, 044906 (2000)
- 730 [54] M.J.Bennett et al. (E878 Collaboration), Phys. Rev. C 58, 1155 (1998).
- 731 [55] G.Ambrosini et al. (NA52 Collaboration), Phys. Lett. B 417, 202 (1998)
- 732 [56] M.I.Abdulhamid et al. (STAR Collaboration), Phys.Rev.Lett. 130 (2023)
733 202301
- 734 [57] D.Zhang (for the STAR Collaboration), Nucl. Phys. A 1005, 121825 (2021).

- 735 [58] I.G.Bearden et al. (BRAHMS Collaboration), Phys. Rev. Lett. 93, 102301,
736 2004.
- 737 [59] F.Videbaek and Ole Hansen, Phys. Rev. C 52 (1995) 2684.
- 738 [60] S.A.Bass et al., Prog. Part. Nucl. Phys. 41 225 (1998).
- 739 [61] B.Hong et al (FOPI Collaboration), Phys. Rev. C 57 (1998) 244.
- 740 [62] J.Bachler et al (NA35 Collaboration), Phys. rev. Lett. 72 (1994) 1419.
- 741 [63] B.B.Back et al (E917 Collaboration), Phys. Rev. Lett. 86 (2001) 1970.
- 742 [64] C.Blume, for the NA49 Collaboration, J. Phys. G 34 (2007) S951.
- 743 [65] M.J.Murray, J. Phys. G 28, 2069 (2002).
- 744 [66] B.Tomasik and U.Heinz, Phys. Rev. C 65, 031902(R) (2002).
- 745 [67] L.P.Csernai and J. I. Kapusta, Phys. Rep. 131, 4 (1986) 223—318.
- 746 [68] S. Z.Belenkij and L.D.Landau, Nuovo Cimento, Supplement 3, 15 (1956).
- 747 [69] G.Poggi et al (FOPI Collaboration), Nucl. Phys. A 586, 755 (1995).
- 748 [70] L.Ahle et al (E802 Collaboration) Phys. Rev. C 60, 064901 (1999).
- 749 [71] T.Anticic et al (NA49 Collaboration), Phys. Rev. C 69, 024902 (2004).
- 750 [72] C.Alt et al (NA49 Collaboration), Phys. Rev. C 77, 024903 (2008).
- 751 [73] T.Anticic et al. (NA49 Collaboration), Phys.Rev.C 85 (2012) 044913
- 752 [74] T.A.Armstrong et al (E864 Collaboration), Phys. Rev. C 61,064908 (2000).
- 753 [75] J.Cleymans, H.Oeschler, K.Redlich and S.Wheaton, Phys. Rev. C 73,
754 034905 (2006).
- 755 [76] L.Adamczyk et al. (STAR Collaboration), Phys. Rev. C 96,044904 (2017).
- 756 [77] K.-J.Sun et al., Phys.Lett.B 774 (2017) 103
- 757 [78] D.Oliinychenko, Nucl.Phys.A 1005 (2021) 121754
- 758 [79] M.I.Abdulhamid et al. (STAR Collaboration), Phys.Rev.Lett. 130 (2023)
759 202301.